

# Siamese Foundation Models for Crystal Structure Prediction

Liming Wu<sup>1</sup>, Wenbing Huang<sup>1, †</sup>, Rui Jiao<sup>3,4</sup>, Jianxing Huang<sup>2</sup>, Liwei Liu<sup>2</sup>, Yipeng Zhou<sup>2</sup>, Hao Sun<sup>1</sup>, Yang Liu<sup>3,4</sup>, Fuchun Sun<sup>3</sup>, Yuxiang Ren<sup>2, †</sup>, and Jirong Wen<sup>1, †</sup>

<sup>1</sup>Gaoling School of Artificial Intelligence, Renmin University of China, Beijing, China

<sup>2</sup>Advance Computing and Storage Lab, Huawei Technologies, Shanghai, China

<sup>3</sup>Department of Computer Science and Technology, Tsinghua University, Beijing, China

<sup>4</sup>Institute for AI Industry Research, Tsinghua University, Beijing, China

<sup>†</sup>Correspondence should be addressed to: hwenbing@ruc.edu.cn; renyuxiang931028@gmail.com;

jrwen@ruc.edu.cn

## ABSTRACT

Crystal Structure Prediction (CSP), which aims to generate stable crystal structures from chemical compositions, represents a critical pathway for discovering novel materials. While structure prediction tasks in other domains, such as proteins, have seen remarkable advancements, CSP remains a relatively underexplored area due to the significantly more complex geometries inherent in crystal structures. In this paper, we propose Siamese foundation models specifically designed to address CSP. Our pretrain-finetune framework, named DAO, comprises two complementary foundation models: DAO-G for structure generation and DAO-P for energy prediction. Experiments on CSP benchmarks (MP-20 and MPTS-52) demonstrate that our DAO-G significantly surpasses state-of-the-art (SOTA) methods across all metrics. Extensive ablation studies further confirm that DAO-G excels in generating diverse polymorphic structures, and the dataset relaxation and energy guidance provided by DAO-P are essential for enhancing DAO-G's performance. When applied to three real-world superconductors ( $\text{CsV}_3\text{Sb}_5$ ,  $\text{Zr}_{16}\text{Rh}_8\text{O}_4$  and  $\text{Zr}_{16}\text{Pd}_8\text{O}_4$ ) that are known to be challenging to analyze, our foundation models achieve accurate critical temperature predictions and structure generations. For instance, on  $\text{CsV}_3\text{Sb}_5$ , DAO-G generates a structure very close to the experimental one with an RMSE of 0.0085; DAO-P predicts the  $T_c$  value with high accuracy (2.26 K vs. the ground-truth value of 2.30 K). In contrast, conventional DFT calculators like Quantum Espresso (QE) only successfully derive the structure of the first superconductor within an acceptable time frame, while the RMSE is nearly 8 times larger, and the computation speed is more than 1000 times slower. These compelling results collectively highlight the potential of our approach for advancing materials science research and development.

## 1 Introduction

Crystals are solid materials composed of atoms, molecules, or ions arranged in a ordered lattice that repeats periodically in three-dimensional space. This highly symmetric, repeating atomic structure endows crystals with unique physical and chemical properties, making them indispensable in advanced technologies and applications, such as the design of semiconductors, ferroelectrics and catalysts [16, 42, 70]. Therefore, Crystal Structure Prediction (CSP), which determines the stable 3D structure of a compound solely from its chemical composition, has remained a fundamental and long-standing pursuit since its conceptual inception in 1950s [21]. The significance of CSP in materials science is analogous to the well-established field of protein structure prediction (or protein folding) in biology. For protein structure prediction, remarkable advancements have been achieved through tools like the AlphaFold series [2, 37, 66]; in contrast, CSP remains a relatively

underexplored task owing to the much more complicated geometries of crystal structures.

Traditional methods for CSP, such as first-principles calculations [25, 39, 64], stochastic sampling [61, 69], and evolutionary optimization [53, 59, 72], generally employ either physics-based or data-driven strategies. These methods, while valuable, are inherently limited by high computational costs and poor scalability with system complexity. In light of the inherent limitations of traditional CSP methods, deep learning has emerged as a powerful technique for achieving a more favorable balance between accuracy and computational cost. Specifically, deep generative models, such as diffusion and flow models [28, 46, 67], have been employed to learn the underlying distribution of crystal structures from existing databases [17, 31, 35, 36, 52, 58, 76]. A key advantage of deep generative models, as highlighted in [35], lies in the denoising process which functions similar to a force field by guiding atom coordinates toward local energy minima, thereby enhancing structural stability. Nevertheless, the State-Of-The-Art (SOTA) models still fall short of achieving satisfactory performance on widely recognized CSP benchmarks like MPTS-52 [33], majorly due to their reliance on domain-specific small datasets for training and the limited generalizability to unseen structures.

One promising approach to enhancing the generalizability of CSP models could involve leveraging *foundation models* [8]. These models, which are pretrained on extensive datasets and finetuned for specific domains, have shown the great power of emergence and homogenization, establishing themselves as a central paradigm in modern AI systems [3, 9, 47, 48]. Inspired by this trend, the development of foundation models for crystals is gaining prominence as a critical research direction in materials science. Existing crystal foundation models can be broadly classified into two categories: supervised and self-supervised pretraining approaches. The first category pretrains models on crystals with energy and force labels, aiming at learning inter-atomic potentials. Representative examples include GNoME [55], DPA-2 [82], MatterSim [79], and MACE-MP-0 [6]. Despite their achievements, these methods are primarily applied to predict the force field of non-stable crystals, which deviates from the objective of CSP that aims to identify stable structures. The second category adopts self-supervised pretraining through either predictive objectives (e.g., feature reconstruction [18, 54, 80] and coordinate denoising [40, 57]) or generative modeling [81]. However, none of these methods specifically targets CSP as a downstream application. Predictive approaches are designed for crystal property prediction, while the generative method MatterGen [81] focuses on general-purpose crystal generation under conditions of desired chemistry, symmetry, and properties.

In this paper, we propose Siamese foundation models specifically designed to tackle CSP. Our proposed framework, termed DAO<sup>1</sup>, comprises two complementary foundation models: DAO-G, which is responsible for deriving stable structures; and DAO-P, which specializes in predicting energy and assisting DAO-G. In particular, DAO-G is a generative model that directly employs CSP as its pretraining task using the diffusion process from DiffCSP [35]. To enable DAO-G to learn from a broader distribution, we incorporate both stable and non-stable structures during pretraining. To facilitate this, we first compile a large pretraining dataset, CrysDB, comprising approximately 940K entries of stable and non-stable crystals with energy annotations. Using CrysDB, we pretrain DAO-G through a two-stage pipeline: in Stage I, DAO-G is trained on all crystals in CrysDB, and in Stage II, it is further trained on a relaxed dataset, where DAO-P acts as an energy predictor to refine non-stable structures into more stable conformations. During the generation process of DAO-G, DAO-P further steers the generated structures via energy guidance. To equip DAO-P with these capabilities, we pretrain it on CrysDB through supervised energy prediction and self-supervised structure generation based on DiffCSP [35]. Notably, Both DAO-P

---

<sup>1</sup>The name DAO draws inspiration from Laozi who described the DAO as the source and ideal of all existence.

and DAO-G are built upon our proposed geometric graph Transformer, *i.e.* Crysformer, which ensures the necessary O(3) and periodic invariance for crystal structures.

We finetune and evaluate our models on two well-known CSP benchmarks, the MP-20 and MPTS-52 datasets [33]. The results demonstrate that our DAO-G significantly surpasses existing SOTA methods across all metrics, validating the effectiveness of our proposed methodology. Extensive ablation studies further confirm that DAO-G excels in generating diverse polymorphic structures, and the dataset relaxation and energy guidance provided by DAO-P are essential for enhancing DAO-G’s performance. As an add-on benefit, our pretrained DAO-P can also be applied to downstream crystal property prediction tasks, achieving SOTA results on four benchmarks and ranking within the top three on the remaining three. Finally, we apply our models to superconductive materials. The pursuit of high-temperature superconductors is motivated by their potential applications in efficient energy transmission and quantum computing [41]. However, the complex structures of superconductive materials have long made their design a formidable challenge. To address this, we finetune DAO-G on a 3D superconductor dataset curated from the SuperCond source [1] and subsequently finetune DAO-P to estimate the  $T_c$  value using augmented structures generated by DAO-G. Remarkably, for three recently discovered superconductors not included in the pretraining or finetuning processes, DAO-G accurately and efficiently predicts their structures. For instance, on  $\text{CsV}_3\text{Sb}_5$  [23], DAO-G generates a structure very close to the experimental one with an RMSE of 0.0085. Simultaneously, DAO-P predicts the  $T_c$  value with high accuracy (2.26 K vs. the ground-truth value of 2.30 K). On the contrary, conventional DFT calculators like Quantum Espresso (QE [26]) only successfully derive the structure of the first superconductor within an acceptable time frame, achieving an RMSE nearly 8 times larger and taking more than 1000 times longer per iteration. These compelling results collectively highlight the potential of our approach for advancing materials science research and development.

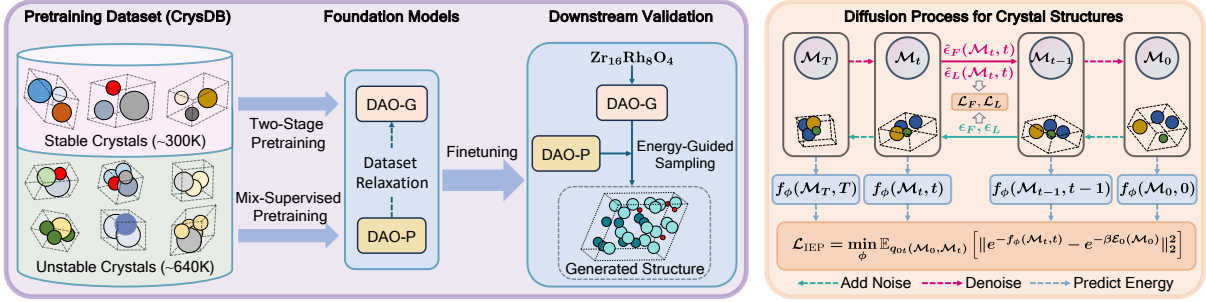
## 2 Results

### 2.1 The Pretrain-Finetune Framework of Our Models

A crystal is represented as  $\mathcal{M} = (\mathbf{A}, \vec{\mathbf{L}}, \mathbf{F})$ , where  $\vec{\mathbf{L}} \in \mathbb{R}^{3 \times 3}$  is the lattice,  $\mathbf{A} \in \mathbb{R}^{1 \times N}$  and  $\mathbf{F} \in [0, 1)^{3 \times N}$  denote the types and fractional coordinates of  $N$  atoms within the lattice, respectively. A crystal  $\mathcal{M}$  is typically considered stable if its energy above the convex hull, namely Ehull, is no greater than 0.08 eV/atom. The CSP task is formulated as learning the distribution  $p(\vec{\mathbf{L}}, \mathbf{F} | \mathbf{A})$ , which generates the stable structure  $(\vec{\mathbf{L}}, \mathbf{F})$  of a crystal given its chemical composition  $\mathbf{A}$ . To tackle CSP, we design Siamese foundation models: DAO-G for structure generation and DAO-P for energy prediction (Fig. 1(a.1)). Both models are built upon a Transformer-like architecture called Crysformer (Fig. 1(b)), which comprises an embedding module, an invariant graph attention module, a gated addition module, and noise/energy output heads. Through its careful design, Crysformer effectively characterizes the geometry of the input crystal while capturing crystallographic symmetries—ensuring that the noise output is equivariant and the energy output is invariant to arbitrary E(3) transformations and periodic translations of the input structure. Further details are provided in Appendices 3.2 and 3.3. We next describe the pretrain-finetune details of DAO-G and DAO-P, separately.

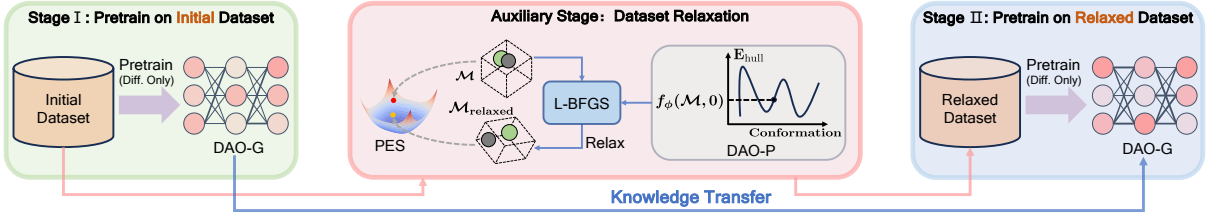
**Pretraining DAO-G** We conduct a two-stage pretraining pipeline for DAO-G (Fig. 1(a.3)). In stage I, in order to learn from a wider distribution, DAO-G is trained to address CSP on all crystals in CrysDB (introduced in § 2.2), which contains a considerable proportion of unstable structures. The

(a) An Overview of Structure Generator (DAO-G) and Energy Predictor (DAO-P)



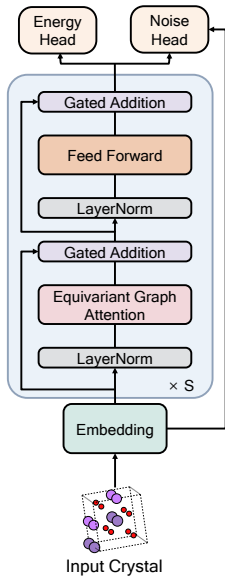
(a.1) The Pipeline of Our Pretrain-Finetune Framework

(a.2) Mix-Supervised Pretraining for DAO-P

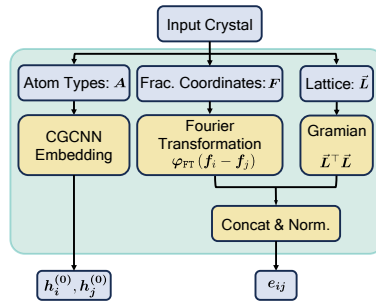


(a.3) Two-Stage Pretraining for DAO-G

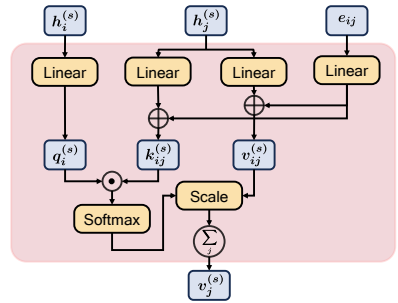
(b) Model Details



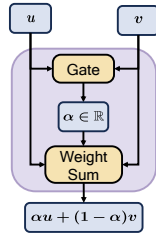
(b.1) Architecture of Crysformer



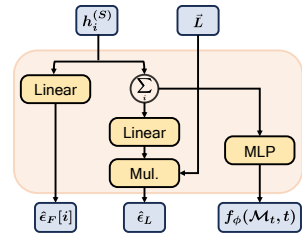
(b.2) Embedding Module



(b.3) Invariant Graph Attention Module



(b.4) Gated Addition Module



(b.5) Noise and Energy Heads

**Figure 1.** A summary of our models: (a) offers an overview of the structure generator (DAO-G) and the energy predictor (DAO-P). (a.1) outlines the pretrain-finetune framework. DAO-G conducts a two-stage pretraining process on CrysDB and DAO-P is pretrained on the same dataset. DAO-P enhances DAO-G by dataset relaxation and energy guidance. (a.2) illustrates the pretraining of DAO-P, which involves the diffusion-based CSP loss to estimate the lattice and fractional noises, and the exponential energy loss aiming at recovering the intermediate energy at each timestep along the diffusion trajectory. (a.3) depicts the two-stage pretraining pipeline of DAO-G. In Stage I, DAO-G is pretrained using the diffusion-based CSP loss on the original dataset. Then, DAO-P is employed to relax unstable structures. In Stage II, DAO-G is continually pretrained on the relaxed dataset. (b) describes the overall architecture and each key component of Crysformer. In DAO-G, only the noise head is utilized, whereas DAO-P incorporates both the noise and energy heads.

CSP task is implemented via a diffusion process proposed by DiffCSP [35], where the noise head of DAO-G requires to estimate the lattice noise  $\epsilon_L(\mathcal{M}_t, t)$  and the fractional noise  $\epsilon_F(\mathcal{M}_t, t)$  of the crystal  $\mathcal{M}_t$  at timestep  $t$  in the denoising process. The inclusion of non-stable structures enables DAO-G to learn from a broader dataset; however, it also introduces a potential bias to unstable regions of the energy landscape, which may limit its effectiveness in generating stable structures. To mitigate this issue, we utilize DAO-P as an efficient energy predictor in place of traditional expensive DFT-based calculators [39], and relax unstable structures with energy values within the range (0.08, 0.5] eV/atom towards more stable configurations. Specifically, DAO-P calculates their energy gradients (i.e., force fields), based on which structure relaxation is subsequently performed using the L-BFGS optimizer [49]. Then, in Stage II, we complete DAO-G’s pretraining by refining the model from Stage I on the relaxed dataset. After training, DAO-G can sample crystal structures by evolving from a prior distribution at  $t = T$  to the data distribution  $t = 0$ . During this sampling process, we further utilize DAO-P as an energy guider to steer the structures generated by DAO-G toward the equilibrium distribution. More details are provided in § 4.3.

Although DAO-G is also a generative model similar to MatterGen [81], it diverges in two critical aspects. First, unlike MatterGen which considers both crystal composition and structure generation as pretraining objectives, DAO-G directly employs CSP as its pretraining task using DiffCSP [35]. Second, while MatterGen pretrains exclusively on stable crystals, our approach incorporates both stable and non-stable structures, allowing the models to learn from a broader distribution.

**Pretraining DAO-P** As mentioned above, DAO-P serves as the energy predictor, playing a dual role in relaxing the pretraining data and guiding the sampling process for DAO-G. To enable this capability, we pretrain DAO-P on CrysDB with two types of loss (Fig. 1(a.2)): (1) the CSP loss applied to the noise head, based on a diffusion process similar to DAO-G, and (2) the energy prediction loss applied to the energy head. The second loss, contributing to energy guidance during the sampling process of DAO-G, requires DAO-P to predict the energy of perturbed crystals at each timestep  $t$  along the diffusion trajectory, namely the intermediate energy  $\mathcal{E}_t(\mathcal{M}_t, t)$ . However, estimating the intermediate energy is more challenging than predicting the energy of equilibrium structures, as ground-truth values for intermediate states are not readily available. To overcome this limitation, we propose an exponential energy loss, whose optimal solution is theoretically proved to converge to the real ground-truth energies under the Boltzmann-constrained modeling [50]. More details are deferred to § 4.4.

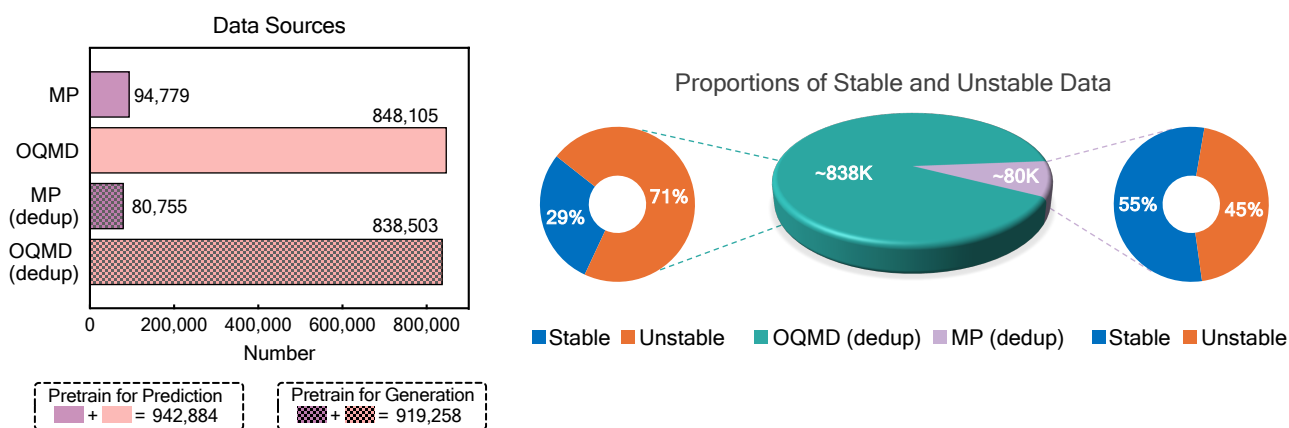
**Finetuning on downstream tasks** After pretraining, DAO-G is well-suited for the CSP task and can be readily finetuned without modifying its architecture (§ 2.3). This seamless transition stems from the close alignment between the pretraining process and the CSP objective. Complementing this, we assess the versatility of DAO-P for predicting properties beyond energy by finetuning it on eight different datasets, each with a unique prediction head (§ 2.4). More importantly, DAO-G and DAO-P can collaborate to facilitate the analyses of superconductors (§ 2.5). In particular, DAO-G is finetuned to generate 3D structures of superconductors, and DAO-P is finetuned to estimate the  $T_c$  value using augmented structures generated by DAO-G.

## 2.2 The Construction of CrysDB

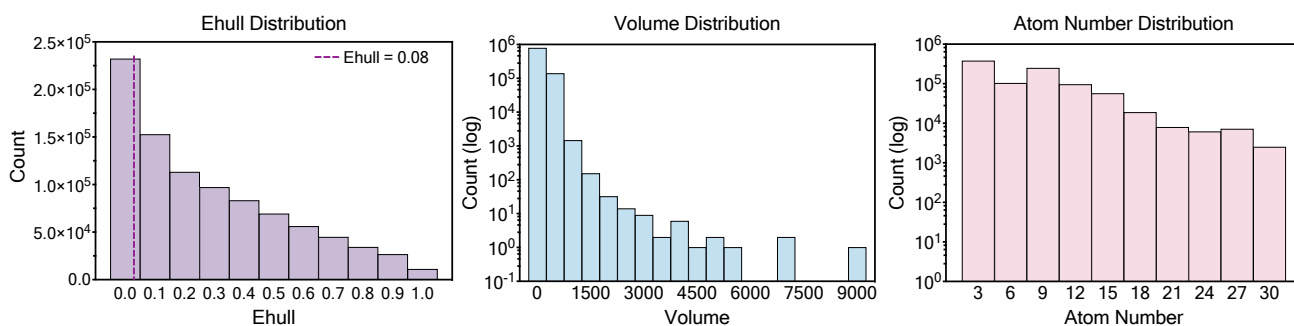
The pretraining dataset CrysDB is sourced from two well-established open-source datasets in the field of crystal research: the Materials Project (MP) [33] and OQMD [38] datasets. Particularly, we collect crystals containing between 3 and 30 atoms, with the Ehull value below 1.0, yielding a total of 94,779 and 838,503 entries from MP and OQMD, respectively, as shown in Fig. 2 (a). In



### (a) Ingredients of the Pretraining Dataset (CrysDB)



### (b) Statistics of CrysDB



### (c) Coverage of Chemical Elements in CrysDB

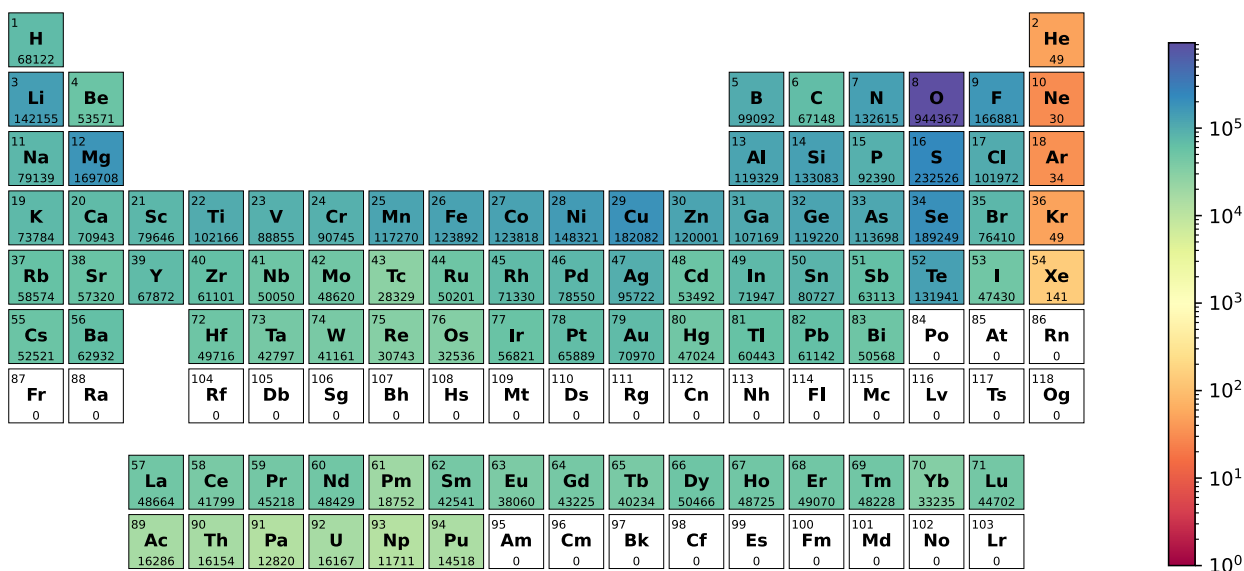


**Figure 2.** Statistics of the pretraining dataset CrysDB: (a) shows the global analyses of the dataset, including the number of entries from MP and OQMD, the statistics of the deduplicated version, and the proportion of stable structures. (b) reports the distributions of Ehull, volume and atom number. (c) presents the elements coverage. It is important to note that the statistics presented in (b) and (c) refer to the deduplicated version of CrysDB used for pretraining DAO-G.

addition, to prevent data leakage on CSP tasks, we exclude any crystals that appear in downstream benchmarks (*i.e.* MP-20 and MPTS-52), resulting in a deduplicated version of CrysDB that consists of 919,258 entries. For a comprehensive description of the dataset curation process, please refer to Appendix 2.5. Fig. 2(a) provides a global analysis of CrysDB, where the right subfigure shows the proportion of stable data from OQMD (29%) and MP (55%). Additional statistical insights into the curated dataset are provided in Fig. 2(b). Specifically, the Ehull distribution reveals that the number of collected crystals monotonically decreases as Ehull increases. The volume distribution extends up to  $9000 \text{ \AA}^3$ , although the majority of crystals have volumes below  $1500 \text{ \AA}^3$ . The distribution of atom number per crystal is relatively uniform across the range of 1 to 30. Furthermore, we summarize the chemical element coverage of our dataset in Fig. 2(c). CrysDB encompasses most groups of the periodic table, excluding heavy radioactive elements ( $Z=84-88$  and  $Z=95-118$ ), with metallic elements constituting the majority.

### 2.3 Accurate Crystal Structure Prediction through the Finetuned DAO-G

We finetune and evaluate DAO-G on two well-recognized benchmarks for studying CSP: MP-20 (with 45,231 crystals) and MPTS-52 (with 40,476 crystals) [33]. Both datasets are derived from the Materials Project (MP), but they differ in complexity; MP-20 limits the number of atoms per crystal to 20, while MPTS-52 extends this to up to 52, encompassing more intricate and diverse structures. Following DiffCSP [35], we utilize the same train/validation/test splits: 27136/9047/9046 for MP-20 and 27380/5000/8096 for MPTS-52, and adopt Match-Rate (MR) and Root-Mean-Square-Error (RMSE) as evaluation metrics. For each reference structure in test time, we report the best MR and RMSE among 1-shot and 20-shot samples generated by DAO-G. We choose the following SOTA methods for comparisons: (1) energy-based model P-cG-SchNet [24]; (2) VAE-based model CDVAE [76]; (3) diffusion-based models, including DiffCSP [35], EquiCSP [44]; (4) flow-based models, such as FlowMM [56] and CrystalFlow [52]. While MatterGen [81] could be modified and adapted for the CSP task here, we exclude it from our comparisons due to data leakage between its pretraining data and the test datasets. To the best of our knowledge, our models are the first foundation models evaluated on these two benchmarks, leveraging the pretrain-finetune paradigm for learning from crystal structures. Notably, both DAO-G and DAO-P used in this section are pretrained on the deduplicated CrysDB.

#### 2.3.1 DAO-G Outperforms SOTA Methods on Two Public Benchmarks

From the results in Table 1, we have the following observations: **(1) Superior Performance of DAO-G.** DAO-G significantly and consistently outperforms other methods on both the MP-20 and MPTS-52 benchmarks. For instance, compared with the best results among all previous methods, there is a clear improvement in MR ( $62.02\% \rightarrow 65.97\%$  on MP-20 and  $22.71\% \rightarrow 32.59\%$  on MPTS-52) and a remarkable reduction in RMSE ( $0.0510 \rightarrow 0.0401$  and  $0.1169 \rightarrow 0.0695$ , respectively), under the 1-shot sampling setting. Similar performance gains are observed for the 20-shot scenario. **(2) Impact of Pretraining/Finetuning.** We implement two variants of DAO-G, one without pretraining: DAO-G (w/o pretrain), and the other one without finetuning: DAO-G (w/o finetune). Compared to these variants, DAO-G demonstrates overall performance improvements, highlighting the essential role of both pretraining and finetuning in enhancing model performance. Excitingly, even without finetuning, DAO-G (w/o finetune) generally outperforms other methods that have been carefully finetuned on the training data of these two benchmarks, except for the MR value on MP-20 in the 1-shot setting. This highlights the effectiveness of large-scale pretraining in enhancing model generalizability. **(3) Efficacy of Crysformer.** DAO-G (w/o pretrain) can be viewed

**Table 1.** CSP performance on MP-20 and MPTS-52. For each metric, the best result of all methods is highlighted in bold, and the best number of previous methods is underlined for clarity. We do not include the 20-shot sampling results for EquiCSP [44] as they were not provided in the original paper. All results of our models are averaged over three runs.

	# of samples	MP-20		MPTS-52	
		Match Rate (%) $\uparrow$	RMSE $\downarrow$	Match Rate (%) $\uparrow$	RMSE $\downarrow$
P-cG-SchNet [24]	1	15.39	0.3762	3.67	0.4115
	20	32.64	0.3018	12.96	0.3942
CDVAE [76]	1	33.90	0.1045	5.34	0.2106
	20	66.95	0.1026	20.79	0.2085
DiffCSP [35]	1	51.49	0.0631	12.19	0.1786
	20	77.93	0.0492	34.02	0.1749
EquiCSP [44]	1	57.39	<u>0.0510</u>	14.85	<u>0.1169</u>
FlowMM [56]	1	61.39	0.0560	17.54	0.1726
	20	75.81	<u>0.0479</u>	34.05	0.1813
CrystalFlow [52]	1	<u>62.02</u>	0.0710	<u>22.71</u>	0.1548
	20	<u>78.34</u>	0.0577	<u>40.37</u>	<u>0.1576</u>
DAO-G (w/o pretrain)	1	51.55	0.0915	17.65	0.1428
	20	76.49	0.0600	35.44	0.1447
DAO-G (w/o finetune)	1	58.38	0.0520	30.32	0.0715
	20	81.96	0.0336	44.98	<b>0.0709</b>
DAO-G	1	<b>65.97</b>	<b>0.0401</b>	<b>32.59</b>	<b>0.0695</b>
	20	<b>82.68</b>	<b>0.0279</b>	<b>46.78</b>	0.0795

as a variant of DiffCSP [35], where the noise model is replaced with our Crysformer. As shown in Table 1, DAO-G (w/o pretrain) performs slightly worse than DiffCSP on MP-20 but outperforms it on MPTS-52, highlighting the effectiveness of Crysformer on generating complex structures. More importantly, Crysformer’s Transformer-like architecture allows it to scale effectively with large-scale pretraining datasets, whereas DiffCSP achieves only moderate results after pretraining (see Appendix 2.1 for details).

### 2.3.2 Involving Unstable Crystals is Essential in Pretraining DAO-G.

During the two-stage pretraining of DAO-G, DAO-P is utilized to relax the pretraining dataset from Stage I to Stage II. Here, we conduct ablation studies to validate the benefits of this strategy. We first assess the energy prediction accuracy of DAO-P, as it is fundamental to the relaxation process. As shown in Fig. 3(d), the Mean-Absolute-Errors (MAEs) of the predicted energies by DAO-P are 0.0260 eV/atom and 0.0514 eV/atom on the test sets of MP-20 and MPTS-52, respectively. Note that DAO-P is NOT even finetuned on these two benchmarks. This accuracy is typically considered acceptable for materials science, suggesting that DAO-P provides a reliable basis for structure relaxation. Besides, Fig. 3(c) illustrates the cumulative energy reduction across different energy bins after relaxation, revealing a clear trend of energy refinement.

We then explore the effect of involving unstable crystals for DAO-G’s pretraining. For this purpose, we consider two ablations of DAO-G without the second stage: DAO-G (Stage I, Stable) that use only stable crystals in deduplicated CrysDB for pretraining, and DAO-G (Stage I) that is pretrained on the full deduplicated CrysDB. For clear reference, the original DAO-G is dubbed as DAO-G (Stage I+II). As visualized in Fig. 3(a), after finetuning, DAO-G (Stage I) outperforms



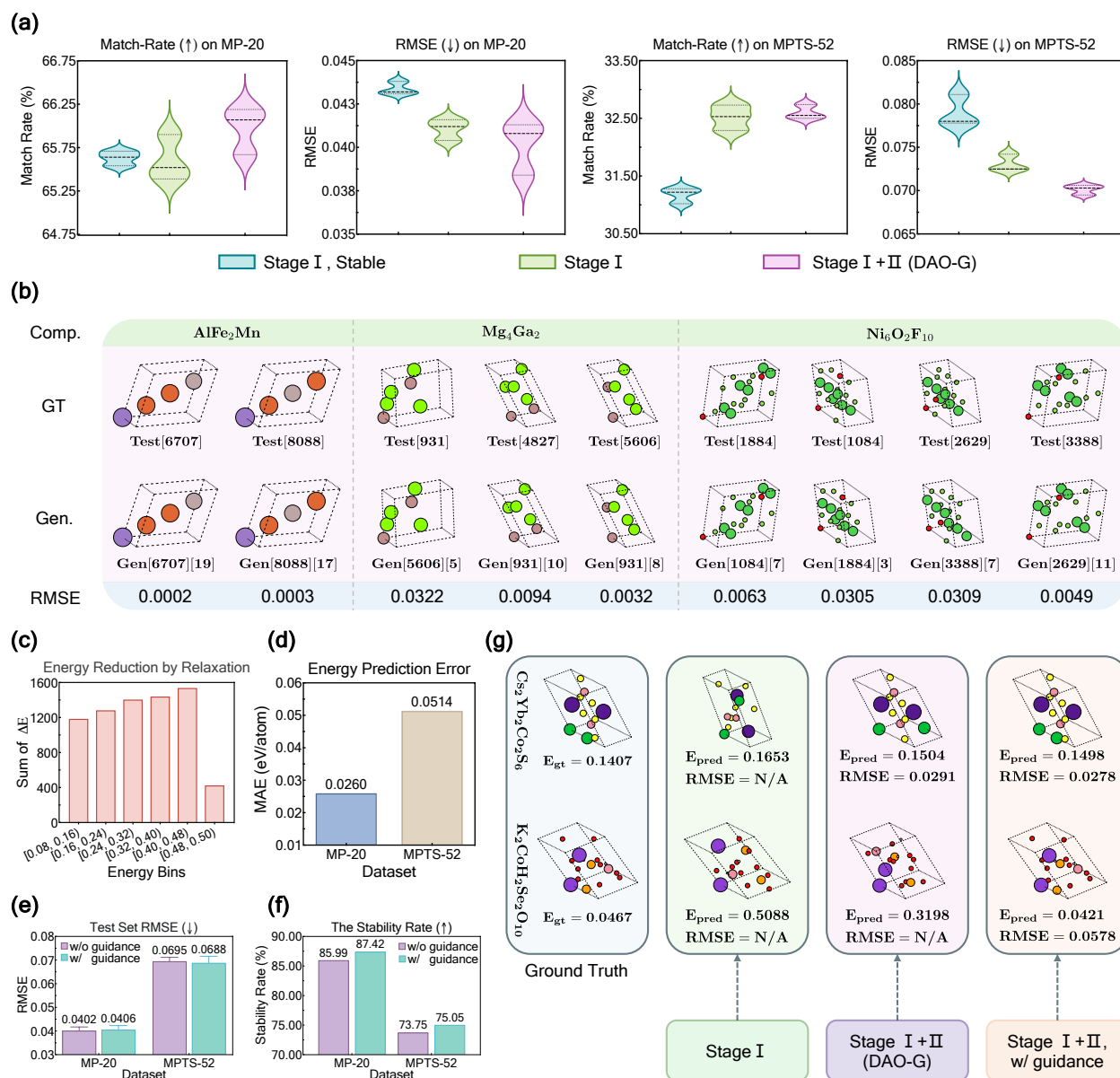


**Figure 3.** In-depth analyses of our models on the CSP benchmarks: **(a)** compares the performance of DAO-G across various configurations. Here, “stage I, Stable” refers to pretraining on the stable-only subset of the deduplicated CrysDB, while “stage I” denotes the first-stage pretraining on the full deduplicated CrysDB. **(b)** gathers the polymorphs (with 2 to 4 conformations) from MP-20, and subsequently compares the generated structures by DAO-G (#samples = 20) with the corresponding ground-truth structures. For clarity, the main abbreviations used in this way: Comp. = Composition, GT = Ground Truth, Gen. = Generation. We provide an example to help understand the bottom annotations: Test[931] denotes the 931st test entry, while Gen[5606][5] represents the fifth of 20 generated samples based on the 5606th entry. **(c)** summarizes energy reduction after conducting relaxation on CrysDB. The term  $\Delta E$  is calculated using normalized energy. **(d)** presents MAEs of energy predictions by DAO-P on the test set of MP-20 and MPTS-52. **(e)** and **(f)** quantifies test RMSE and stability rate between the models with and without energy guidance. **(g)** visualizes two examples from MPTS-52, showing the benefits of generation with energy guidance. N/A denotes the failed match.

DAO-G (Stage I, Stable) in most cases, suggesting that directly incorporating unstable data during pretraining enhances DAO-G’s performance. We now compare DAO-G (Stage I+Stage II) with DAO-G (Stage I). On MP-20, DAO-G (Stage I+Stage II) achieves improved MR and lower RMSE, though with a slight increase in RMSE variance. On MPTS-52, it maintains comparable MR while significantly reducing RMSE and lowering variance for both metrics. These results highlight the effectiveness of conducting data relaxation in the two-stage pretraining. We present more details in Appendix 2.1.

### 2.3.3 DAO-G excels in generating polymorphic structures

In crystallography, polymorphism refers to the phenomenon in which a compound can crystallize into multiple distinct crystal structures. These polymorphs often exhibit diverse physicochemical properties, underscoring the importance of identifying the optimal structures for specific applications. Developing a generative model capable of capturing the structural diversity of polymorphs is crucial yet challenging. Such a model would need to account for the geometric variations in atomic arrangements and energetics that give rise to different polymorphic forms. To evaluate whether DAO-G can effectively generate polymorphs, we select several representative groups of polymorphs from the MP-20 test set, with the number of conformations ranging from 2 to 4. The results, as shown in Fig. 3(b), demonstrate that DAO-G successfully generates diverse conformations for the same chemical composition, achieving remarkably low RMSE values in each case. For example, for the case of  $\text{Ni}_6\text{O}_2\text{F}_{10}$ , which has 4 distinct conformations in the test set, we generate 20 samples for each conformation, resulting in a total of 80 ( $= 20 \times 4$ ) generated structures in total. We can observe that all the 4 different conformations are hit successfully by the generated structures, with correspondingly low RMSE values of 0.0063, 0.0305, 0.0309, and 0.0049, respectively. This demonstrates the model’s ability to accurately capture and replicate the structural diversity of polymorphic systems.

### 2.3.4 Energy-Guided Sampling by DAO-P Contributes to Higher-Stability Generation

As outlined in § 2.1, DAO-P is pretrained to predict the intermediate energy of noise-added crystals along the diffusion path. To harness this capability, we apply DAO-P as the energy guider and implement energy-guided sampling for the generation process of DAO-G, following the methodology introduced in [35]. Further details are provided in § 4.5. Here, we conduct quantitative analyses from three perspectives. First, we report the test RMSE on MP-20 and MPTS-52 in Fig. 3(e). It is observed that incorporating energy guidance yields comparable RMSE on MP-20, but a lower RMSE ( $0.0695 \rightarrow 0.0688$ ) on the more difficult dataset MPTS-52, suggesting that energy guidance is particularly beneficial for generating complex crystal structures. Second, we examine the stability rate of the generated structures in Fig. 3(f). Clearly, DAO-G (w/ guidance) exhibits higher stability rates compared to the counterpart without guidance on both MP-20 and MPTS-52, namely, 87.42% vs. 85.99% and 75.05% vs. 73.75%, respectively. It confirms our hypothesis that energy guidance does promote structural stability. Finally, we visualize two specific examples in Fig. 3(g) to provide further insight into the impact of energy guidance. For the first example,  $\text{Cs}_2\text{Yb}_2\text{Co}_2\text{S}_6$ , while DAO-G achieves relatively low RMSE and energy values compared to the one-stage model, the incorporation of energy guidance further enhances performance. Specifically, the RMSE decreases from 0.0291 to 0.0278, and the predicted energy is reduced from 0.1504 eV/atom to 0.1498 eV/atom. For the second example, we choose a considerably more complex crystal,  $\text{K}_2\text{Co}_2\text{H}_4\text{Se}_2\text{O}_{10}$ . In this case, only the energy-guided DAO-G successfully matches the ground truth, as demonstrated by its low RMSE of 0.0578 and its precise energy prediction relative to the ground truth (0.0421 vs. 0.0467). With the inclusion of energy guidance, DAO-G achieves a

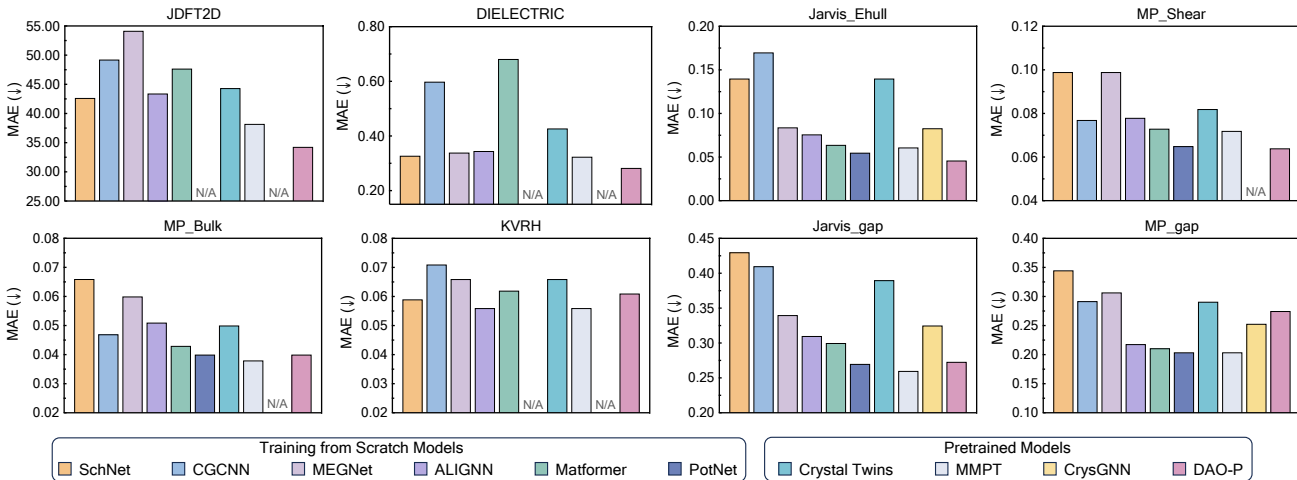


**Figure 4.** The performance of DAO-P for crystal property prediction is evaluated on eight datasets. The compared baselines include models both with and without pretraining, with the results directly taken from their respective papers. For baselines where the corresponding experiments were not conducted in the original paper, the results are denoted as N/A.

significant energy reduction of 86.8%, decreasing from 0.3198 to 0.0421. The results above support the critical role of energy guidance in handling complex crystal structures and achieving both structural and energetic accuracy.

## 2.4 Accurate Crystal Property Prediction via the Finetuned DAO-P

In previous experiments, DAO-P has functioned as an energy predictor, assisting DAO-G through dataset relaxation and sampling guidance. We now explore whether the pretraining of DAO-P on energy prediction provides a robust foundation for predicting a broader spectrum of material properties. Specifically, we first pretrain DAO-P on the full version of CrysDB and then finetune it on eight representative datasets selected from three widely-used benchmarks: Matbench [22], JARVIS-3D [14] and MP [33]. To ensure consistency and comparability, we adopt the experimental settings described in Matformer [78] for JARVIS-3D and MP, and utilize the default settings for the Matbench datasets. For comparison, we choose two categories of SOTA methods on these benchmarks: models without pretraining [10, 12, 45, 65, 75, 78], and models with pretraining [18, 54, 80]. We quantify the accuracy using the MAE metric.

The results are presented in Fig. 4. Notably, DAO-P outperforms previous approaches on half of the evaluated datasets and achieves competitive results on the remaining datasets, with the exception of MP\_gap. Across these datasets, DAO-P consistently ranks among the top three performers, demonstrating its robustness and generalization capability. Particularly striking is the significant performance improvement on Jarvis\_Ehull, where DAO-P achieves a 16.3% increase over the second-best method. Furthermore, the effectiveness of DAO-P in few-shot learning scenarios is demonstrated by its outstanding performance on the JDFT2D dataset, which contains only 636 instances. For more detailed comparisons, see Appendix 2.2. In conclusion, DAO-P is not limited to energy prediction; it can be adapted to predict a wide range of material properties with appropriate finetuning datasets. Moreover, the principle of energy guidance can be extended to other properties. For instance, DAO-P could be utilized to bias the generation process toward structures with enhanced Shear Modulus. This underscores the remarkable flexibility and versatility

of DAO-P as a key component of our framework.

## 2.5 DAO-G and DAO-P Demonstrate Significant Potential for Superconductor Analysis

In this section, we evaluate the capabilities of DAO-G and DAO-P in analyzing superconductors. Specifically, we focus on two key tasks: the prediction of 3D crystal structures and the estimation of the critical temperature  $T_c$ . It is noteworthy that predicting the structure of superconductors is more complex than that of ordinary crystals due to their intricate structural features and the sensitivity of superconductivity to structural variations. Determining the critical temperature presents an even greater challenge. For conventional superconductors, this requires the application of Bardeen-Cooper-Schrieffer (BCS) theory [5] to model electron-phonon interactions. For unconventional superconductors, other theoretical models are necessary. These complexities highlight the need of DAO-G and DAO-P, which can address these challenges through their effectiveness in structure generation and property prediction.

As illustrated in Fig. 5(a), we finetune our pretrained models using the publicly available SuperCon3D dataset [11], which includes 1017 ordered superconductors with known structures and 748 ordered superconductors without structural information. Fig. 5(b) provides a visualization of  $T_c$  distribution for both categories, exhibiting a broad range of values. We first finetune DAO-G on the subset of entries with structures and then use it to generate structures (1-shot sampling) for the remaining 748 compositions. The 1017 structural subset is randomly divided into 5 folds, each further augmented with the generated structures of the 748 entries. Finally, we finetune DAO-P to predict  $T_c$  using the original dataset and its augmented version, respectively, under the 5-fold-cross-validation setting. Fig. 5(c) shows that augmenting DAO-P with generated structures consistently improves performance across all 5 folds, reducing the average MAE (logK) from 0.747 to 0.709. These results confirm the strong potential of DAO-G in practical scenarios where structural information is unavailable and demonstrate that incorporating the structures generated by DAO-G can enhance the performance of DAO-P.

To validate the practicability of our models on real-world systems, we further conduct evaluations on three recently discovered superconductors:  $\text{CsV}_3\text{Sb}_5$  [23],  $\text{Zr}_{16}\text{Rh}_8\text{O}_4$  [73] and  $\text{Zr}_{16}\text{Pd}_8\text{O}_4$  [73]. These three superconductors are unseen during both the pretraining and finetuning processes, thereby avoiding the risk of data leakage. The ensemble of the five DAO-P models, finetuned under the aforementioned 5-fold cross-validation setting, is leveraged to predict the  $T_c$  values. Remarkably, the absolute errors are all minor, being 0.04 (K), 0.26 (K) and 0.04 (K), as shown in Fig. 5(d, first row). In addition, we employ the finetuned DAO-G to generate crystal structures for each superconductor and present the most accurate ones of 20-shot sampling in Fig. 5(d, second row). Notably, determining the structures of these three superconductors are known to be challenging. For instance,  $\text{CsV}_3\text{Sb}_5$  exhibits a unique kagome lattice, where V atoms form the kagome planes, while Cs and Sb atoms constitute the interspersing layers. DAO-G achieves an impressively low RMSE of 0.0085, accurately recovering its experimental structure. For the second superconductor  $\text{Zr}_{16}\text{Pd}_8\text{O}_4$ , it exhibits  $\eta$ -carbide structure (space group  $Fd\bar{3}m$ ) with intricate atomic arrangements, such as rigid Wyckoff site occupancy and geometrically frustrated stella quadrangula lattices. DAO-G successfully generates the structure with an RMSE of 0.0172. In contrast,  $\text{Zr}_{16}\text{Rh}_8\text{O}_4$  exhibits a minor change in lattice constant ( $\sim 0.5\%$ ) when substituting Rh for Pd, which, yet, significantly affects its superconducting properties, such as increasing  $T_c$  from 2.73 K to 3.73 K. Remarkably, DAO-G is still capable of resolving this subtle structural change, achieving a low RMSE of 0.0212. To further investigate the relationship between sample size and accuracy, we report the best RMSE of generating 1, 5, 10, 15 and 20 samples by DAO-G in the last row of Fig. 5(d). We find that

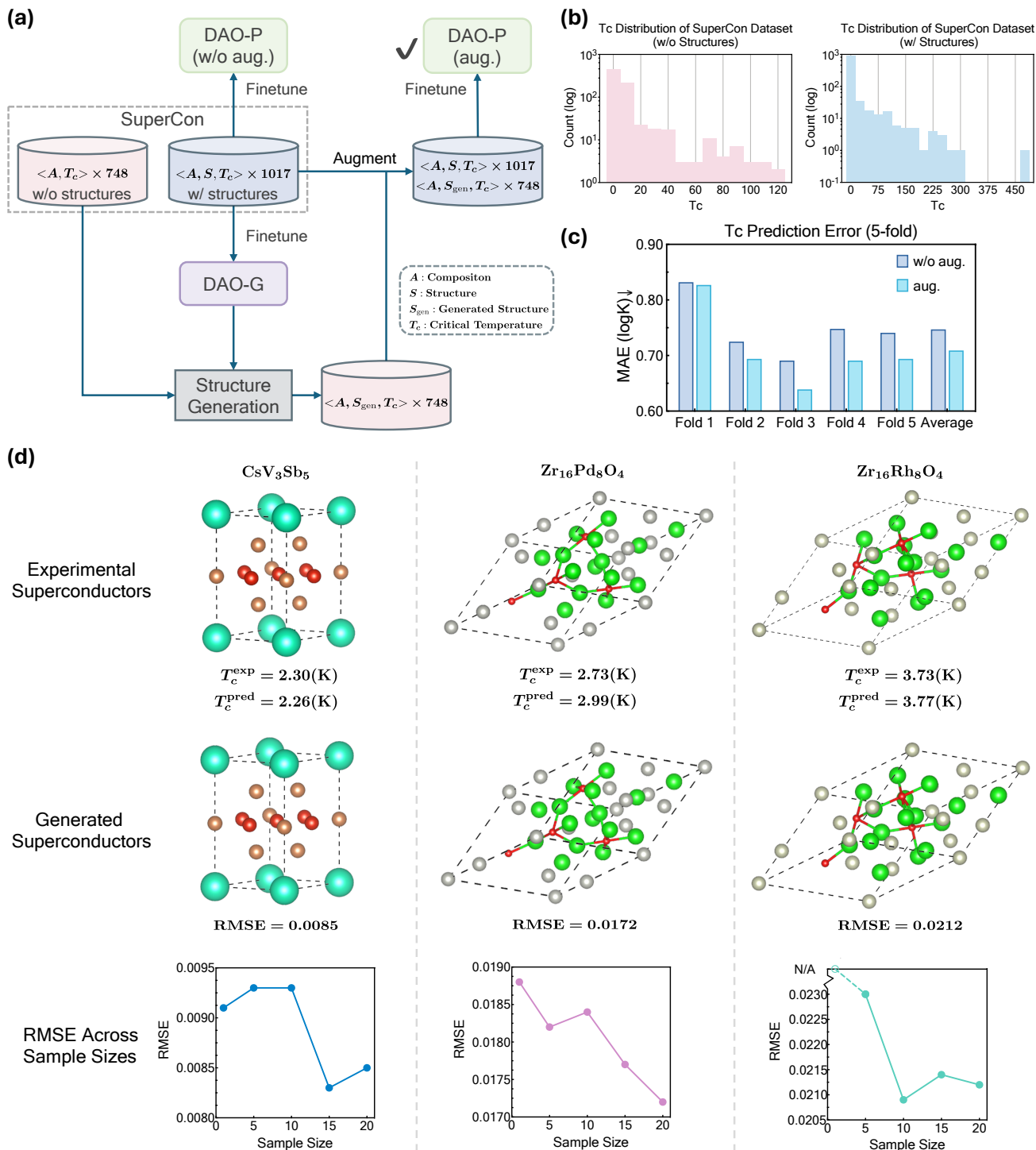


**Figure 5.** Experiments on superconductors: (a) depicts the finetuning process of DAO-P and DAO-G on the SuperCon3D dataset [11], in which 3D structures are known for a subset of materials. (b) presents the distributions of the critical temperature ( $T_c$ ). (c) displays the  $T_c$  prediction error evaluated with the 5-fold cross-validation setting. (d) shows the results of the three recently discovered real-world superconductors, all of which are excluded from the pretraining and finetuning processes. We employ DAO-P (aug.) for  $T_c$  prediction and DAO-G for structure generation, subsequently analyzing how the RMSE evolves as the sample size grows. The hollow point (#sample = 1) in the last curve figure for the third superconductor signifies the failed match.



accurate structures can be generated for the first two superconductors with even 1-shot sampling, and for all three superconductors with just 5-shot sampling. These results demonstrate the sampling efficiency of DAO-G.

We also try to derive the structures of the three superconductors using the DFT-based calculator, Quantum Espresso (QE) [26]. Unfortunately, when starting from random initial structures, QE fails to produce meaningful results, highlighting the inherent challenge of this task. To enable QE to function, we instead initialize the structures by adding random noise to the experimental structures. Even with this adjustment, QE only yields reasonable structures for CsV<sub>3</sub>Sb<sub>5</sub>, failing to do so for the other two superconductors. Among 10 random runs, the best RMSE achieved by QE is 0.0637, which is significantly worse than our result of 0.0085 obtained with 20-shot sampling. Furthermore, in this scenario, QE takes about 4 hours over 50 iterations, whereas our DAO-G completes 1000 sampling iterations in just several minutes. Comprehensive details are provided in Appendix 2.3.

### 3 Conclusion and Discussion

This paper presents Siamese foundation models specifically designed to address CSP challenges. Our pretrain-finetune framework, named DAO, comprises two complementary foundation models: DAO-G for structure generation and DAO-P for energy prediction, both of which are built upon a proposed geometric Transformer, Crysformer. For the pretraining, we construct a crystal pretraining dataset (i.e., CrysDB) of about 940K entries with structures and the corresponding energy labels. The key feature of our approach is the ability to leverage generative pretraining and effectively handle unstable data through a dedicated relaxation process and energy guidance sampling, leading to improved generation of stable structures.

We rigorously evaluate the performance of our method across a variety of downstream tasks. In CSP evaluation, DAO-G achieves SOTA results on both MP-20 and MPTS-52 datasets, highlighting its ability to generate stable crystal structures accurately. Ablation studies validate the benefits of our proposed dataset relaxation and energy guidance for improving the generative performance. Meanwhile, DAO-G is proved to be effective to generate polymorphic structures. Moreover, DAO-P demonstrates exceptional transferability in property prediction tasks, outperforming existing methods on four out of eight datasets. It is also worth mentioning that experiments on superconductors provide further evidence of the synergistic interaction and mutual performance enhancement between DAO-G and DAO-P, demonstrating the practicability of our models on real-world systems.

In a nutshell, our approach has proven to be highly effective in both accurate structure generation and flexible property prediction. The development of DAO contributes to the growing body of research on co-designing generative and predictive models, highlighting the potential for their synergistic interactions. Meanwhile, it offers a practical solution for effectively leveraging the vast unstable data available in materials databases. Looking ahead, future work could explore more robust and efficient property prediction models, as well as extending the framework of DAO to wider scientific modalities, such as proteins and genes, to develop more powerful and versatile foundation models.

### 4 Methods

A crystal possesses a repeating structural unit that extends infinitely throughout 3D space. The unit comprises a lattice and atoms situated within it. The periodicity of a crystal lattice is embodied in three vectors,  $\vec{L} = [\vec{l}_1, \vec{l}_2, \vec{l}_3] \in \mathbb{R}^{3 \times 3}$ , each defining a direction along which the structure repeats. Within the lattice, the chemical composition is characterized as atom types  $\mathbf{A} = [\mathbf{a}_1, \mathbf{a}_2, \dots, \mathbf{a}_N] \in$

$\mathbb{R}^{1 \times N}$ , and the atom Cartesian coordinates are denoted as  $\vec{\mathbf{X}} = [\vec{\mathbf{x}}_1, \vec{\mathbf{x}}_2, \dots, \vec{\mathbf{x}}_N] \in \mathbb{R}^{3 \times N}$ , where  $N$  is the number of atoms. Fractional coordinates,  $\mathbf{F} = \vec{\mathbf{L}}^{-1} \vec{\mathbf{X}} = [\mathbf{f}_1, \mathbf{f}_2, \dots, \mathbf{f}_N] \in [0, 1)^{3 \times N}$ , offer an alternative format to represent atom locations. This representation inherently places atoms within the lattice, which is particularly useful for crystal structure generation. We employ fractional coordinates in this paper, as opposed to Cartesian coordinates. As a result, a crystal can be shown as  $\mathcal{M} = (\mathbf{A}, \vec{\mathbf{L}}, \mathbf{F})$ .

#### 4.1 Equivariant Diffusion Models for Crystals

Inspired by DiffCSP [35], our diffusion-based pretraining can be formulated as  $p(\vec{\mathbf{L}}, \mathbf{F} | \mathbf{A})$ , that is, generating lattice and fractional coordinates given the chemical composition. This distribution needs to adhere to  $O(3)$  invariance and periodical translation invariance, which for simplicity we collectively refer to as *OP-invariance*. It suggests that lattice rotation and coordinates translation do not affect the generation process. The notation of  $\mathcal{M}_t$  denotes a crystal at timestep  $t$  in the diffusion process. A typical diffusion model consists of a forward process and a backward process.

In the forward process, different noise schedules are adopted for lattice and fractional coordinates. Particularly, we employ a noise addition strategy used in DDPM [28] for the lattice, which is modeled as:

$$q(\vec{\mathbf{L}}_t | \vec{\mathbf{L}}_0) = \mathcal{N} \left( \vec{\mathbf{L}}_t | \sqrt{\bar{\alpha}_t} \vec{\mathbf{L}}_0, (1 - \bar{\alpha}_t) \mathbf{I} \right), \quad \bar{\alpha}_t = \prod_{s=1}^t \alpha_s, \quad (1)$$

where  $\alpha_s$  is scale of the noise added at timestep  $s$ .

In contrast, for fractional coordinates, we employ a Score-Matching method [67] and instantiate the forward process using the Wrapped Normal (WN) Distribution [19]:

$$q(\mathbf{F}_t | \mathbf{F}_0) \propto \sum_{\mathbf{Z} \in \mathbb{Z}^{3 \times N}} \exp \left( \frac{-\|\mathbf{F}_t - \mathbf{F}_0 + \mathbf{Z}\|_F^2}{2\gamma_t^2} \right), \quad (2)$$

where,  $\gamma_t$  is sampled from an exponential scheduler. The use of WN distribution provides a significant advantage in reflecting the periodic nature of crystal structures [35].

During the backward process, we seek to reconstruct the added noise  $\epsilon_t^L$  for lattice, and reconstruct the score for fractional coordinates. The corresponding training objectives are implemented as:

$$\mathcal{L}_L = \mathbb{E}_{\epsilon_t^L \sim \mathcal{N}(0, \mathbf{I}), t \sim \mathcal{U}(1, T)} \left[ \|\hat{\epsilon}_L(\mathcal{M}_t, t) - \epsilon_t^L\|_2^2 \right], \quad (3)$$

$$\mathcal{L}_F = \mathbb{E}_{\mathbf{F}_t \sim q(\mathbf{F}_t | \mathbf{F}_0), t \sim \mathcal{U}(1, T)} \left[ \lambda_t \|\hat{\epsilon}_F(\mathcal{M}_t, t) - \nabla_{\mathbf{F}_t} \log q(\mathbf{F}_t | \mathbf{F}_0)\|_2^2 \right]. \quad (4)$$

where,  $\hat{\epsilon}_L(\mathcal{M}_t, t)$  is the predicted noise for lattice,  $\hat{\epsilon}_F(\mathcal{M}_t, t)$  is the predicted score for coordinates and  $\lambda_t$  is estimated by Monte-Carlo sampling. For the pretraining of DAO-G, the training objective is the combination of  $\mathcal{L}_L$  and  $\mathcal{L}_F$ .

Importantly, to achieve the distribution OP-invariant,  $\hat{\epsilon}_L$  is supposed to be  $O(3)$  equivariant and  $\hat{\epsilon}_F$  needs to satisfy periodical translation invariance. In the following section (§ 4.2), we introduce a powerful graph Transformer to output the noises  $\hat{\epsilon}_L$  and  $\hat{\epsilon}_F$ , which retains these symmetries, capable of effectively capturing the intricacies of crystal structures and accomplishing the denoising process.

## 4.2 Equivariant Graph Transformer: Crysformer

Recognizing the proven power of the Transformer architecture [68] in pretraining [51], we adopt graph Transformer (Fig. 1(b.1)) as our foundational building block to replace the GNN-based architecture used in DiffCSP [35]. Our Crysformer mainly consists of four modules: an embedding module for initializing node and edge features; an invariant graph attention module for capturing inter-node interactions; a gated addition module for residual connections; and the noise and energy prediction heads for outputting predictions. Subsequently, we present a comprehensive description of each module.

**Embedding Module.** As shown in Fig. 1(b.2), we firstly initialize the node features  $\mathbf{H}^{(0)} = [\mathbf{h}_1^{(0)}, \mathbf{h}_2^{(0)}, \dots, \mathbf{h}_N^{(0)}] \in \mathbb{R}^{d_h \times N}$  with CGCNN embeddings [75]. Prior to feeding the crystal into the model, we precompute edge features, represented as  $\mathbf{E} = \{\mathbf{e}_{ij}\} \in \mathbb{R}^{d_e \times N_e}$ .  $d_e$  and  $N_e$  are the dimension of edge features and the number of edges, respectively. Specifically, the edge feature between atom  $i$  and  $j$  is calculated by:

$$\mathbf{e}_{ij} = \text{Normalization} \left( \vec{\mathbf{L}}^\top \vec{\mathbf{L}} \parallel \varphi_{\text{FT}}(\mathbf{f}_i - \mathbf{f}_j) \right), \quad (5)$$

where  $\parallel$  denotes concatenation and  $\varphi_{\text{FT}}$  is Fourier Transform (FT) to ensure the edge feature satisfy translation invariant [35].

**Invariant Graph Attention Module.** Furthermore, we design the  $s$ -th attention layer (Fig. 1(b.3)) as  $\mathbf{Z}^{(s)} = \text{ATT}(\mathbf{H}^{(s-1)}, \mathbf{E}) = [\mathbf{z}_0^{(s)}, \mathbf{z}_1^{(s)}, \dots, \mathbf{z}_N^{(s)}]$ , with four parametric MLPs:  $\varphi_q, \varphi_k, \varphi_v$  and  $\varphi_e$ . The details are as follows:

$$\left. \begin{aligned} \mathbf{q}_i^{(s)} &= \varphi_q(\mathbf{h}_i^{(s-1)}) \\ \mathbf{k}_{ij}^{(s)} &= \varphi_k(\mathbf{h}_j^{(s-1)}) + \varphi_e(\mathbf{e}_{ij}) \\ \mathbf{v}_{ij}^{(s)} &= \varphi_v(\mathbf{h}_j^{(s-1)}) + \varphi_e(\mathbf{e}_{ij}) \end{aligned} \right\} \implies \mathbf{z}_i^{(s)} = \sum_{j \neq i}^N \text{softmax}_j \left( \frac{\langle \mathbf{q}_i^{(s)}, \mathbf{k}_{ij}^{(s)} \rangle}{\sqrt{d_h}} \right) \mathbf{v}_{ij}^{(s)}, \quad (6)$$

In fact, we use multi-head attention in our model, in line with the standard Transformer [68].

**Gated Addition Module.** We also utilize residual connection in the model design. A primary difference arises from the using of Gated Residual (GR) connection (Fig. 1(b.4)), written as:

$$\text{GR}(\mathbf{x}, \psi(\mathbf{x})) = \alpha \mathbf{x} + (1 - \alpha) \psi(\mathbf{x}), \quad \alpha = \varphi_g(\mathbf{x}, \psi(\mathbf{x}), \mathbf{x} - \psi(\mathbf{x})) \in \mathbb{R}, \quad (7)$$

where  $\psi(\mathbf{x})$  is a function with respect to  $\mathbf{x}$  and  $\varphi_g$  is a MLP used to learn the gating coefficient  $\alpha$ . Compared to the vanilla residue connection [27], gated addition provides a gate mechanism to control the strengths of the input and layer output, which is more flexible and robust.

**Crysformer Block.** Moreover, we adopt PreNorm (PRN) layer normalization in our architecture [77], as opposed to the PostNorm employed in the vanilla Transformer design. With the aforementioned several techniques, we can build a Crysformer block as:

$$\mathbf{Z}^{(s)} = \text{GR} \left( \mathbf{H}^{(s-1)}, \text{ATT} \left( \text{PRN} \left( \mathbf{H}^{(s-1)} \right), \mathbf{E} \right) \right), \quad (8)$$

$$\mathbf{H}^{(s)} = \text{GR} \left( \mathbf{Z}^{(s)}, \text{FFN} \left( \text{PRN} \left( \mathbf{Z}^{(s-1)} \right) \right) \right). \quad (9)$$

Here, FFN is the feedforward layer. Our Crysformer is a stack of  $S$  blocks, where  $\mathbf{H}^{(S)}$  contains node features extracted from the final layer. We conduct average pooling of the node features to obtain the crystal feature  $\bar{\mathbf{h}} = \frac{1}{N} \sum_{i=1}^N \mathbf{h}_i^{(S)}$ . The notations  $\bar{\mathbf{h}}_t$  and  $\mathbf{H}_t^{(S)}$  denote the crystal feature and the set of node features at timestep  $t$ , with  $t = 0$  by default if not explicitly specified. The node feature  $\mathbf{h}_i^{(S)}$  is designed to be O(3)-invariant, and the proof is provided in Appendix 3.2.

**Noise and Energy Heads.** Then, the learned node and crystal features can be used to predict both the lattice noise  $\hat{\epsilon}_L(\mathcal{M}_t, t)$  and the fractional coordinates score  $\hat{\epsilon}_F(\mathcal{M}_t, t)$ . Concretely, as illustrated in Fig. 1(b.5), we feed the node features into a neural network  $\varphi_F$  to predict the fractional coordinates score, through  $\hat{\epsilon}_F(\mathcal{M}_t, t)[i, :] = \varphi_F(\mathbf{H}_t^{(S)}[i, :])$ , where  $[i, :]$  selects the  $i$ -th atom. Since the lattice belongs to the entire crystal, we use the crystal feature as input to another neural network  $\varphi_L$ . We further multiply the output of  $\varphi_L$  by the lattice to make sure that the predicted noise meets O(3)-equivariance, yielding  $\hat{\epsilon}_L(\mathcal{M}_t, t) = \vec{\mathbf{L}}\varphi_L(\bar{\mathbf{h}}_t)$ . Meanwhile, for the energy prediction, we implement the energy head  $\varphi_E$  with a two-layer MLP and output the energy using  $\bar{\mathbf{h}}_t$  as the input, that is,  $\varphi_E(\bar{\mathbf{h}}_t)$ . More details are shown in Appendix 3.3.

### 4.3 Two-Stage Pretraining for DAO-G

We now provide a detailed explanation of each stage involved in DAO-G pretraining and the corresponding dataset relaxation procedure.

#### 4.3.1 Stage I: Generative Pretraining on the Original Dataset

The first stage of our pretraining strategy involves training DAO-G on the full CrysDB (dedup), which encompasses both stable and a considerable proportion of unstable crystals. This broad training dataset, combined with the diffusion process proposed by DiffCSP [35], allows DAO-G to learn a more generalized representation of crystal structures, capturing the variability present in both stable and unstable crystals. Specifically, different noise schedules are adopted (§ 4.1), where we choose the standard DDPM [28] for lattice generation, while for fractional coordinates we employ a Score-Matching method [67] and instantiate the forward process using the Wrapped Normal (WN) Distribution [19]. During training, DAO-G learns to predict the lattice noise  $\epsilon_L(\mathcal{M}_t, t)$  and fractional coordinate noise  $\epsilon_F(\mathcal{M}_t, t)$ , guided by the loss functions defined in Eqs. (3) and (4). By pretraining DAO-G on both stable and unstable data in the first stage, we aim to capture a wider distribution of crystal structures.

#### 4.3.2 Auxiliary Stage: Dataset Relaxation

Despite the benefits of incorporating unstable data, employing them as input can bias the generation towards energetically unfavorable regions of the energy landscape. A straightforward idea is to relax the unstable data for quality improvement using DFT [39], which is a widely used and reliable method for relaxing biochemical structures, but its high computational cost presents a significant challenge. As a more efficient alternative, we propose a machine learning-based approach for the relaxation of unstable crystals. Specifically, using the pretrained DAO-P, we can predict the energy  $f_\phi(\mathcal{M}, 0)$  for a given crystal  $\mathcal{M}$  and compute the corresponding structural energy gradient (i.e.,  $\nabla_{\vec{\mathbf{L}}}f_\phi(\mathcal{M}, 0)$  and  $\nabla_{\mathbf{F}}f_\phi(\mathcal{M}, 0)$ ), which are subsequently used as input for L-BFGS [49] to guide the optimization process towards a minimal energy state. Actually, the L-BFGS optimization is performed using the PyTorch library [62] with the following hyperparameter configurations: `max_iter = 5`, `lr = 1.0`. Notably, we only relax data whose Ehull ranges from 0.08 eV/atom to 0.5 eV/atom. Here, the choice of relaxation algorithm is flexible, and other similar gradient-based optimization methods are also suitable.

#### 4.3.3 Stage II: Diffusion Model Refinement

After relaxation, we combine the remaining original data ( $\text{Ehull} \in [0, 0.08) \cup (0.5, 1.0]$  eV/atom) with the relaxed data to form a new pretraining dataset, whose size is same to the original one. In the second stage, we refine DAO-G by continuing training on the relaxed dataset. Using this dataset and a reduced learning rate, we resume training the model initialized with the parameters from

the first stage and employ the same training losses. This allows for a refinement of the denoising process based on the improved data quality.

The hyperparameters used in the two-stage pretraining are presented in Table 9. Upon completion of the training-relaxation-training paradigm, the foundation model DAO-G is fully pretrained and ready for finetuning on CSP datasets to specialize in the generation of stable crystal structures.

#### 4.4 Mix-Supervised Pretraining for DAO-P

Beyond dataset relaxation for DAO-G pretraining, DAO-P also provides crucial energy guidance during the sampling process of DAO-G (will be introduced in § 4.5). For this functionality, DAO-P is required to predict the energy of perturbed crystals at each timestep  $t$  along the diffusion trajectory, namely the intermediate energy  $\mathcal{E}_t(\mathcal{M}_t, t)$ . Therefore, we pretrain DAO-P using a hybrid loss function that combines self-supervised diffusion losses (Eqs. (3) and (4), as in DAO-G pretraining) and a supervised intermediate energy prediction loss (Eq. (10)). Given the energy predicted by Crysformer’s energy head (§ 4.2), we denote the collective parameters as  $\phi$  and the resulting predicted energy as  $f_\phi(\mathcal{M}_t, t)$ . A key challenge in supervised training is the lack of readily accessible energy labels  $\mathcal{E}_t(\mathcal{M}_t)$  for timesteps  $t > 0$ . Previous approaches attempted to solve it by employing techniques such as MSE supervision [4, 34], posterior sampling [29] and contrastive prediction [50]. Nevertheless, these methods suffer from either inaccurate prediction or computational instability [50, 71]. Here, we carefully design a loss function with martingale policy [74] to train  $f_\phi(\mathcal{M}_t, t)$  exactly, demonstrated by:

**Proposition 1** (Intermediate Energy Prediction). *Given  $\mathcal{E}_t(\mathcal{M}_t) = -\log \mathbb{E}_{q_{0t}(\mathcal{M}_0|\mathcal{M}_t)}[e^{-\beta\mathcal{E}_0(\mathcal{M}_0)}]$  representing the true energy [50], we aim to learn a parameterized function  $f_\phi(\mathcal{M}_t, t)$  to approximate  $\mathcal{E}_t(\mathcal{M}_t)$ . Then  $f_\phi(\mathcal{M}_t, t)$  can be obtained as the solution to the following optimization problem:*

$$\phi^* = \arg \min_{\phi} \mathbb{E}_{q_{0t}(\mathcal{M}_0, \mathcal{M}_t)} [\|e^{-f_\phi(\mathcal{M}_t, t)} - e^{-\beta\mathcal{E}_0(\mathcal{M}_0)}\|_2^2]. \quad (10)$$

We refer to this loss function as  $\mathcal{L}_{\text{IEP}}$ , which is proved in Appendix 3.1.

#### 4.5 Energy-Guided Sampling

Although we incorporate dataset relaxation during training to combat the instability arising from unstable data, this does not fully eliminate the issue. Therefore, we further address this challenge during sampling, drawing inspiration from the Energy-Based Models (EBMs).

We can learn the relationship between data distribution and the corresponding energy  $\mathcal{E}_0(\mathcal{M}_0)$  from Boltzmann distribution [43]:  $\mathcal{M}_0 \sim \exp(-\beta\mathcal{E}_0(\mathcal{M}_0))/Z$ , where  $\beta$  is the temperature coefficient and  $Z$  is the normalization constant. It indicates that data points with higher energy are less likely to occur. Importantly, the Boltzmann distribution exhibits a useful property: its log-likelihood is equivalent to the negative energy gradient with respect to data, which acts as a force field, driving updates towards lower energy configurations, and consequently, greater stability. Thus, the instability issue of unstable data incorporation is mitigated. This helpful conclusion motivates us to design an EBM to guide the sampling process.

The goal of those standard diffusion models is to learn the data distribution  $q_0(\mathcal{M}_0)$ . Rather, we aim to train the energy-guided diffusion model to learn a modified distribution that is proportional to the original distribution weighted by the Boltzmann factor, namely,  $p_0(\mathcal{M}_0) \propto q_0(\mathcal{M}_0)e^{-\beta\mathcal{E}_0(\mathcal{M}_0)}$ . On this basis, CEP [50] further proposes that: if the conditional distributions are equal, i.e.,  $p_t(\mathcal{M}_t|\mathcal{M}_0) = q_t(\mathcal{M}_t|\mathcal{M}_0)$ , then the marginal distribution  $p_t(\mathcal{M}_t) \propto q_t(\mathcal{M}_t)e^{-\beta\mathcal{E}_t(\mathcal{M}_t, t)}$ , where



$\mathcal{E}_t(\mathcal{M}_t)$  is the intermediate energy predicted by the pretrained DAO-P. The energy-guided distribution  $p_t(\mathcal{M}_t)$  adheres to equilibrium distribution better and its score is more interesting and informative, computed by:

$$\underbrace{\nabla_{\mathcal{M}_t} \log p_t(\mathcal{M}_t)}_{\text{energy-guided score}} = \underbrace{\nabla_{\mathcal{M}_t} \log q_t(\mathcal{M}_t)}_{\text{original score}} - \underbrace{\beta \nabla_{\mathcal{M}_t} \mathcal{E}_t(\mathcal{M}_t)}_{\text{energy guidance}}. \quad (11)$$

Details of the implementation are introduced in Appendix 2.4.

## 4.6 Evaluation Metrics

We assess structure generation performance with two metrics: Match Rate (MR), which measures the percentage of successful matches between generated and ground truth structures, and Root Mean Square Error (RMSE), which quantifies the deviation in atomic coordinates. Property prediction is evaluated using Mean Absolute Error (MAE) between predicted and labeled properties. While for superconductor property prediction, we use MAE calculated on the logarithm of the  $T_c$  values.

## 5 Author contributions statement

L.W. and W.H. drafted the manuscript; L.W. and R.J. developed the code and conducted the experiments; L.W. organized the experimental results; W.H., J.H., L.L., Y.Z., H.S., Y.L., F.S., Y.R., and J.W. provided technical support; W.H., Y.R., and J.W. supervised the research. All authors reviewed the final version of the manuscript.

## References

1. Supercon database. <https://doi.org/10.48505/nims.3739>, 2022.
2. Josh Abramson, Jonas Adler, Jack Dunger, Richard Evans, Tim Green, Alexander Pritzel, Olaf Ronneberger, Lindsay Willmore, Andrew J Ballard, Joshua Bambrick, et al. Accurate structure prediction of biomolecular interactions with alphafold 3. *Nature*, 630(8016):493–500, 2024.
3. Josh Achiam, Steven Adler, Sandhini Agarwal, Lama Ahmad, Ilge Akkaya, Florencia Leoni Aleman, Diogo Almeida, Janko Altschmidt, Sam Altman, Shyamal Anadkat, et al. Gpt-4 technical report. *arXiv preprint arXiv:2303.08774*, 2023.
4. Fan Bao, Min Zhao, Zhongkai Hao, Peiyao Li, Chongxuan Li, and Jun Zhu. Equivariant energy-guided sde for inverse molecular design. In *The eleventh international conference on learning representations*, 2022.
5. John Bardeen, Leon N Cooper, and J Robert Schrieffer. Microscopic theory of superconductivity. *Physical Review*, 106(1):162, 1957.
6. Ilyes Batatia, Philipp Benner, Yuan Chiang, Alin M Elena, Dávid P Kovács, Janosh Riebesell, Xavier R Advincula, Mark Asta, Matthew Avaylon, William J Baldwin, et al. A foundation model for atomistic materials chemistry. *arXiv preprint arXiv:2401.00096*, 2023.
7. Guenter Bergerhoff, R Hundt, R Sievers, and ID Brown. The inorganic crystal structure data base. *Journal of chemical information and computer sciences*, 23(2):66–69, 1983.

8. Rishi Bommasani, Drew A Hudson, Ehsan Adeli, Russ Altman, Simran Arora, Sydney von Arx, Michael S Bernstein, Jeannette Bohg, Antoine Bosselut, Emma Brunskill, et al. On the opportunities and risks of foundation models. *arXiv preprint arXiv:2108.07258*, 2021.
9. Tom Brown, Benjamin Mann, Nick Ryder, Melanie Subbiah, Jared D Kaplan, Prafulla Dhariwal, Arvind Neelakantan, Pranav Shyam, Girish Sastry, Amanda Askell, et al. Language models are few-shot learners. *Advances in neural information processing systems*, 33:1877–1901, 2020.
10. Chi Chen, Weike Ye, Yunxing Zuo, Chen Zheng, and Shyue Ping Ong. Graph networks as a universal machine learning framework for molecules and crystals. *Chemistry of Materials*, 31(9):3564–3572, 2019.
11. Pin Chen, Luoxuan Peng, Rui Jiao, Qing Mo, Zhen Wang, Wenbing Huang, Yang Liu, and Yutong Lu. Learning superconductivity from ordered and disordered material structures. *Advances in Neural Information Processing Systems*, 37:108902–108928, 2025.
12. Kamal Choudhary and Brian DeCost. Atomistic line graph neural network for improved materials property predictions. *npj Computational Materials*, 7(1):185, 2021.
13. Kamal Choudhary, Irina Kalish, Ryan Beams, and Francesca Tavazza. High-throughput identification and characterization of two-dimensional materials using density functional theory. *Scientific reports*, 7(1):5179, 2017.
14. Kamal Choudhary, Kevin F Garrity, Andrew CE Reid, Brian DeCost, Adam J Biacchi, Angela R Hight Walker, Zachary Trautt, Jason Hattrick-Simpers, A Gilad Kusne, Andrea Centrone, et al. The joint automated repository for various integrated simulations (jarvis) for data-driven materials design. *npj computational materials*, 6(1):173, 2020.
15. Kamal Choudhary, Daniel Wines, Kangming Li, Kevin F Garrity, Vishu Gupta, Aldo H Romero, Jaron T Krogel, Kayahan Saritas, Addis Fuhr, Panchapakesan Ganesh, et al. Jarvis-leaderboard: a large scale benchmark of materials design methods. *npj Computational Materials*, 10(1):93, 2024.
16. W Cochran. Crystal stability and the theory of ferroelectricity. *Advances in Physics*, 9(36):387–423, 1960.
17. Callum J Court, Batuhan Yildirim, Apoorv Jain, and Jacqueline M Cole. 3-d inorganic crystal structure generation and property prediction via representation learning. *Journal of Chemical Information and Modeling*, 60(10):4518–4535, 2020.
18. Kishalay Das, Bidisha Samanta, Pawan Goyal, Seung-Cheol Lee, Satadeep Bhattacharjee, and Niloy Ganguly. Crysgnn: Distilling pre-trained knowledge to enhance property prediction for crystalline materials. In *Proceedings of the AAAI Conference on Artificial Intelligence*, volume 37, pages 7323–7331, 2023.
19. Valentin De Bortoli, Emile Mathieu, Michael Hutchinson, James Thornton, Yee Whye Teh, and Arnaud Doucet. Riemannian score-based generative modelling. *Advances in Neural Information Processing Systems*, 35:2406–2422, 2022.

20. Maarten De Jong, Wei Chen, Thomas Angsten, Anubhav Jain, Randy Notestine, Anthony Gamst, Marcel Sluiter, Chaitanya Krishna Ande, Sybrand Van Der Zwaag, Jose J Plata, et al. Charting the complete elastic properties of inorganic crystalline compounds. *Scientific data*, 2(1):1–13, 2015.
21. Gautam R Desiraju. Cryptic crystallography. *Nature materials*, 1(2):77–79, 2002.
22. Alexander Dunn, Qi Wang, Alex Ganose, Daniel Dopp, and Anubhav Jain. Benchmarking materials property prediction methods: the matbench test set and automatminer reference algorithm. *npj Computational Materials*, 6(1):138, 2020.
23. Jun Ge, Pinyuan Wang, Ying Xing, Qiangwei Yin, Anqi Wang, Jie Shen, Hechang Lei, Ziqiang Wang, and Jian Wang. Charge-4 e and charge-6 e flux quantization and higher charge superconductivity in kagome superconductor ring devices. *Physical Review X*, 14(2):021025, 2024.
24. Niklas WA Gebauer, Michael Gastegger, Stefaan SP Hessmann, Klaus-Robert Müller, and Kristof T Schütt. Inverse design of 3d molecular structures with conditional generative neural networks. *Nature communications*, 13(1):973, 2022.
25. Paolo Giannozzi, Stefano Baroni, Nicola Bonini, Matteo Calandra, Roberto Car, Carlo Cavazzoni, Davide Ceresoli, Guido L Chiarotti, Matteo Cococcioni, Ismaila Dabo, et al. Quantum espresso: a modular and open-source software project for quantum simulations of materials. *Journal of physics: Condensed matter*, 21(39):395502, 2009.
26. Paolo Giannozzi, Oliviero Andreussi, Thomas Brumme, Oana Bunau, M Buongiorno Nardelli, Matteo Calandra, Roberto Car, Carlo Cavazzoni, Davide Ceresoli, Matteo Cococcioni, et al. Advanced capabilities for materials modelling with quantum espresso. *Journal of physics: Condensed matter*, 29(46):465901, 2017.
27. Kaiming He, Xiangyu Zhang, Shaoqing Ren, and Jian Sun. Deep residual learning for image recognition. In *Proceedings of the IEEE conference on computer vision and pattern recognition*, pages 770–778, 2016.
28. Jonathan Ho, Ajay Jain, and Pieter Abbeel. Denoising diffusion probabilistic models. *Advances in neural information processing systems*, 33:6840–6851, 2020.
29. Jonathan Ho, Tim Salimans, Alexey Gritsenko, William Chan, Mohammad Norouzi, and David J Fleet. Video diffusion models. *Advances in Neural Information Processing Systems*, 35:8633–8646, 2022.
30. Emiel Hoogeboom, Victor Garcia Satorras, Clément Vignac, and Max Welling. Equivariant diffusion for molecule generation in 3d. In *International conference on machine learning*, pages 8867–8887. PMLR, 2022.
31. Jianjun Hu, Wenhui Yang, and Edirisuriya M Dilanga Siriwardane. Distance matrix-based crystal structure prediction using evolutionary algorithms. *The Journal of Physical Chemistry A*, 124(51):10909–10919, 2020.

32. Lei Huang, Hengtong Zhang, Tingyang Xu, and Ka-Chun Wong. Mdm: Molecular diffusion model for 3d molecule generation. In *Proceedings of the AAAI Conference on Artificial Intelligence*, volume 37, pages 5105–5112, 2023.
33. A Jain, SP Ong, G Hautier, W Chen, WD Richards, S Dacek, S Cholia, D Gunter, D Skinner, G Ceder, et al. The materials project: a materials genome approach to accelerating materials innovation. *apl mater* 1: 011002, 2013.
34. Michael Janner, Yilun Du, Joshua Tenenbaum, and Sergey Levine. Planning with diffusion for flexible behavior synthesis. In *International Conference on Machine Learning*, pages 9902–9915. PMLR, 2022.
35. Rui Jiao, Wenbing Huang, Peijia Lin, Jiaqi Han, Pin Chen, Yutong Lu, and Yang Liu. Crystal structure prediction by joint equivariant diffusion. *Advances in Neural Information Processing Systems*, 36, 2024.
36. Rui Jiao, Wenbing Huang, Yu Liu, Deli Zhao, and Yang Liu. Space group constrained crystal generation. In *The Twelfth International Conference on Learning Representations*, 2024.
37. John Jumper, Richard Evans, Alexander Pritzel, Tim Green, Michael Figurnov, Olaf Ronneberger, Kathryn Tunyasuvunakool, Russ Bates, Augustin Židek, Anna Potapenko, et al. Highly accurate protein structure prediction with alphafold. *nature*, 596(7873):583–589, 2021.
38. Scott Kirklin, James E Saal, Bryce Meredig, Alex Thompson, Jeff W Doak, Muratahan Aykol, Stephan Rühl, and Chris Wolverton. The open quantum materials database (oqmd): assessing the accuracy of dft formation energies. *npj Computational Materials*, 1(1):1–15, 2015.
39. Walter Kohn and Lu Jeu Sham. Self-consistent equations including exchange and correlation effects. *Physical review*, 140(4A):A1133, 1965.
40. Teddy Koker, Keegan Quigley, Will Spaeth, Nathan C Frey, and Lin Li. Graph contrastive learning for materials. *arXiv preprint arXiv:2211.13408*, 2022.
41. Thaddeus D Ladd, Fedor Jelezko, Raymond Laflamme, Yasunobu Nakamura, Christopher Monroe, and Jeremy Lloyd O’Brien. Quantum computers. *nature*, 464(7285):45–53, 2010.
42. Jane H Larsen and Ib Chorkendorff. From fundamental studies of reactivity on single crystals to the design of catalysts. *Surface Science Reports*, 35(5-8):163–222, 1999.
43. EM Lifshitz and LP Pitaevskii. Statistical physics, course of theoretical physics. In *Part 2: Theory of the Condensed State*, volume 9. Butterworth-Heinemann Pergamon, London, 1980.
44. Peijia Lin, Pin Chen, Rui Jiao, Qing Mo, Cen Jianhuan, Wenbing Huang, Yang Liu, Dan Huang, and Yutong Lu. Equivariant diffusion for crystal structure prediction. In *Forty-first International Conference on Machine Learning*, 2024.
45. Yuchao Lin, Keqiang Yan, Youzhi Luo, Yi Liu, Xiaoning Qian, and Shuiwang Ji. Efficient approximations of complete interatomic potentials for crystal property prediction. In *International Conference on Machine Learning*, pages 21260–21287. PMLR, 2023.

46. Yaron Lipman, Ricky TQ Chen, Heli Ben-Hamu, Maximilian Nickel, and Matt Le. Flow matching for generative modeling. *arXiv preprint arXiv:2210.02747*, 2022.
47. Aixin Liu, Bei Feng, Bin Wang, Bingxuan Wang, Bo Liu, Chenggang Zhao, Chengqi Deng, Chong Ruan, Damai Dai, Daya Guo, et al. Deepseek-v2: A strong, economical, and efficient mixture-of-experts language model. *arXiv preprint arXiv:2405.04434*, 2024.
48. Aixin Liu, Bei Feng, Bing Xue, Bingxuan Wang, Bochao Wu, Chengda Lu, Chenggang Zhao, Chengqi Deng, Chenyu Zhang, Chong Ruan, et al. Deepseek-v3 technical report. *arXiv preprint arXiv:2412.19437*, 2024.
49. Dong C Liu and Jorge Nocedal. On the limited memory bfgs method for large scale optimization. *Mathematical programming*, 45(1):503–528, 1989.
50. Cheng Lu, Huayu Chen, Jianfei Chen, Hang Su, Chongxuan Li, and Jun Zhu. Contrastive energy prediction for exact energy-guided diffusion sampling in offline reinforcement learning. In *International Conference on Machine Learning*, pages 22825–22855. PMLR, 2023.
51. Shengjie Luo, Tianlang Chen, Yixian Xu, Shuxin Zheng, Tie-Yan Liu, Liwei Wang, and Di He. One transformer can understand both 2d & 3d molecular data. In *The Eleventh International Conference on Learning Representations*, 2022.
52. Xiaoshan Luo, Zhenyu Wang, Jian Lv, Lei Wang, Yanchao Wang, and Yanming Ma. Crystalflow: A flow-based generative model for crystalline materials. *arXiv preprint arXiv:2412.11693*, 2024.
53. Andriy O Lyakhov, Artem R Oganov, Harold T Stokes, and Qiang Zhu. New developments in evolutionary structure prediction algorithm uspeX. *Computer Physics Communications*, 184(4):1172–1182, 2013.
54. Rishikesh Magar, Yuyang Wang, and Amir Barati Farimani. Crystal twins: self-supervised learning for crystalline material property prediction. *npj Computational Materials*, 8(1):231, 2022.
55. Amil Merchant, Simon Batzner, Samuel S Schoenholz, Muratahan Aykol, Gwoon Cheon, and Ekin Dogus Cubuk. Scaling deep learning for materials discovery. *Nature*, 624(7990):80–85, 2023.
56. Benjamin Kurt Miller, Ricky T. Q. Chen, Anuroop Sriram, and Brandon M Wood. FlowMM: Generating materials with riemannian flow matching. In *Forty-first International Conference on Machine Learning*, 2024.
57. Alexander New, Nam Q Le, Michael Pekala, and Christopher D Stiles. Self-supervised learning for crystal property prediction via denoising. In *ICML 2024 AI for Science Workshop*, 2021.
58. Asma Nouria, Nataliya Sokolovska, and Jean-Claude Crivello. CrystalGAN: learning to discover crystallographic structures with generative adversarial networks. *arXiv preprint arXiv:1810.11203*, 2018.
59. Artem R Oganov and Colin W Glass. Crystal structure prediction using ab initio evolutionary techniques: Principles and applications. *The Journal of chemical physics*, 124(24), 2006.



60. Shyue Ping Ong, William Davidson Richards, Anubhav Jain, Geoffroy Hautier, Michael Kocher, Shreyas Cholia, Dan Gunter, Vincent L Chevrier, Kristin A Persson, and Gerbrand Ceder. Python materials genomics (pymatgen): A robust, open-source python library for materials analysis. *Computational Materials Science*, 68:314–319, 2013.
61. Jean Pannetier, J Bassas-Alsina, Juan Rodriguez-Carvajal, and Vincent Caignaert. Prediction of crystal structures from crystal chemistry rules by simulated annealing. *Nature*, 346(6282): 343–345, 1990.
62. Adam Paszke, Sam Gross, Francisco Massa, Adam Lerer, James Bradbury, Gregory Chanan, Trevor Killeen, Zeming Lin, Natalia Gimelshein, Luca Antiga, et al. Pytorch: An imperative style, high-performance deep learning library. *Advances in neural information processing systems*, 32, 2019.
63. Ioannis Petousis, David Mrdjenovich, Eric Ballouz, Miao Liu, Donald Winston, Wei Chen, Tanja Graf, Thomas D Schladt, Kristin A Persson, and Fritz B Prinz. High-throughput screening of inorganic compounds for the discovery of novel dielectric and optical materials. *Scientific data*, 4(1):1–12, 2017.
64. Chris J Pickard and RJ Needs. Ab initio random structure searching. *Journal of Physics: Condensed Matter*, 23(5):053201, 2011.
65. Kristof Schütt, Pieter-Jan Kindermans, Huziel Enoc Saucedo Felix, Stefan Chmiela, Alexandre Tkatchenko, and Klaus-Robert Müller. Schnet: A continuous-filter convolutional neural network for modeling quantum interactions. *Advances in neural information processing systems*, 30, 2017.
66. Andrew W Senior, Richard Evans, John Jumper, James Kirkpatrick, Laurent Sifre, Tim Green, Chongli Qin, Augustin Židek, Alexander WR Nelson, Alex Bridgland, et al. Improved protein structure prediction using potentials from deep learning. *Nature*, 577(7792):706–710, 2020.
67. Yang Song, Conor Durkan, Iain Murray, and Stefano Ermon. Maximum likelihood training of score-based diffusion models. *Advances in neural information processing systems*, 34:1415–1428, 2021.
68. A Vaswani. Attention is all you need. *Advances in Neural Information Processing Systems*, 2017.
69. David J Wales. Energy landscapes and structure prediction using basin-hopping. *Modern Methods of Crystal Structure Prediction*, pages 29–54, 2010.
70. Chengliang Wang, Huanli Dong, Lang Jiang, and Wenping Hu. Organic semiconductor crystals. *Chemical Society Reviews*, 47(2):422–500, 2018.
71. Lihao Wang, Yuning Shen, Yiqun Wang, Huizhuo Yuan, Yue Wu, Quanquan Gu, et al. Protein conformation generation via force-guided se (3) diffusion models. In *Forty-first International Conference on Machine Learning*, 2024.
72. Yanchao Wang, Jian Lv, Li Zhu, and Yanming Ma. Calypso: A method for crystal structure prediction. *Computer Physics Communications*, 183(10):2063–2070, 2012.

73. Yuto Watanabe, Akira Miura, Chikako Moriyoshi, Aichi Yamashita, and Yoshikazu Mizuguchi. Observation of superconductivity and enhanced upper critical field of  $\eta$ -carbide-type oxide  $\text{Zr}_4\text{Pd}_2\text{O}$ . *Scientific Reports*, 13(1):22458, 2023.
74. David Williams. *Probability with martingales*. Cambridge university press, 1991.
75. Tian Xie and Jeffrey C Grossman. Crystal graph convolutional neural networks for an accurate and interpretable prediction of material properties. *Physical review letters*, 120(14):145301, 2018.
76. Tian Xie, Xiang Fu, Octavian-Eugen Ganea, Regina Barzilay, and Tommi S. Jaakkola. Crystal diffusion variational autoencoder for periodic material generation. In *International Conference on Learning Representations*, 2022.
77. Ruibin Xiong, Yunchang Yang, Di He, Kai Zheng, Shuxin Zheng, Chen Xing, Huishuai Zhang, Yanyan Lan, Liwei Wang, and Tieyan Liu. On layer normalization in the transformer architecture. In *International Conference on Machine Learning*, pages 10524–10533. PMLR, 2020.
78. Keqiang Yan, Yi Liu, Yuchao Lin, and Shuiwang Ji. Periodic graph transformers for crystal material property prediction. *Advances in Neural Information Processing Systems*, 35:15066–15080, 2022.
79. Han Yang, Chenxi Hu, Yichi Zhou, Xixian Liu, Yu Shi, Jielan Li, Guanzhi Li, Zekun Chen, Shuizhou Chen, Claudio Zeni, et al. Mattersim: A deep learning atomistic model across elements, temperatures and pressures. *arXiv preprint arXiv:2405.04967*, 2024.
80. Haomin Yu, Yanru Song, Jilin Hu, Chenjuan Guo, and Bin Yang. A crystal-specific pre-training framework for crystal material property prediction. *arXiv preprint arXiv:2306.05344*, 2023.
81. Claudio Zeni, Robert Pinsler, Daniel Zügner, Andrew Fowler, Matthew Horton, Xiang Fu, Sasha Shysheya, Jonathan Crabbé, Lixin Sun, Jake Smith, et al. Mattergen: a generative model for inorganic materials design. *arXiv preprint arXiv:2312.03687*, 2023.
82. Duo Zhang, Xinzijian Liu, Xiangyu Zhang, Chengqian Zhang, Chun Cai, Hangrui Bi, Yiming Du, Xuejian Qin, Jiameng Huang, Bowen Li, et al. Dpa-2: Towards a universal large atomic model for molecular and material simulation. *arXiv preprint arXiv:2312.15492*, 2023.

# Supplementary Information: Siamese Foundation Models for Crystal Structure Prediction

Liming Wu<sup>1</sup>, Wenbing Huang<sup>1, †</sup>, Rui Jiao<sup>3,4</sup>, Jianxing Huang<sup>2</sup>, Liwei Liu<sup>2</sup>, Yipeng Zhou<sup>2</sup>, Hao Sun<sup>1</sup>, Yang Liu<sup>3,4</sup>, Fuchun Sun<sup>3</sup>, Yuxiang Ren<sup>2, †</sup>, and Jirong Wen<sup>1, †</sup>

<sup>1</sup>Gaoling School of Artificial Intelligence, Renmin University of China, Beijing, China

<sup>2</sup>Advance Computing and Storage Lab, Huawei Technologies, Shanghai, China

<sup>3</sup>Department of Computer Science and Technology, Tsinghua University, Beijing, China

<sup>4</sup>Institute for AI Industry Research, Tsinghua University, Beijing, China

<sup>†</sup>Correspondence should be addressed to: hwenbing@ruc.edu.cn; renyuxiang931028@gmail.com; jrwen@ruc.edu.cn

## Contents

<b>1 Preliminaries</b>	<b>2</b>
1.1 Diffusion Models	2
1.2 Equivariance and Invariance	2
<b>2 Experimental Details</b>	<b>2</b>
2.1 Raw Results of Structure Generation	2
2.2 Raw Results of Property Prediction	3
2.3 More Results of Superconductor Validation	3
2.3.1 Implementation Details	3
2.3.2 DFT Results for Three Real-World Superconductors	4
2.4 Implementation of Energy-Guided Sampling	5
2.5 Pretraining Dataset Deduplication	6
2.6 Downstream Datasets Introduction	6
2.7 Hyperparameters	8
2.8 Configurations of Finetuning	8
2.9 Visualization of the Diffusion Process	8
<b>3 Theoretical Analysis</b>	<b>8</b>
3.1 Derivation of the Intermediate Energy Prediction Loss	9
3.2 Invariance of the learned Node Features	10
3.3 Equivariance of the Noise Output	10

# 1 Preliminaries

## 1.1 Diffusion Models

Diffusion process unfolds in two stages: a forward pass that adds noise to the data and a backward pass focused on denoising. During the forward process, noise is progressively added to the original data sample until it conforms to a predefined distribution at timestep  $T$ , commonly chosen to be a standard normal distribution. Denoising (the backward process) often requires the model to predict the noise introduced at each timestep, as in DDPM [28]. Alternatively, methods like Score-Matching [67] aim to predict the gradient of the log-likelihood, also known as the score  $s_\theta$ . When utilizing diffusion models for the generation of geometric objects, particularly those in three dimensions, it is imperative to incorporate knowledge of the inherent symmetry present in the data to avoid generating unrealistic or physically implausible structures. For instance, several studies [30, 32] have incorporated E(3) equivariance into their diffusion model architectures for molecular generation. In the same vein, our diffusion-based model for crystal structure pretraining needs to account for this fundamental constraint, which is discussed in Appendix 1.2.

## 1.2 Equivariance and Invariance

We investigate the equivariance of geometric models under the group  $\mathfrak{G}$ , specifically analyzing how the transformation of the input structure affect the output. A function  $f : \mathcal{X} \rightarrow \mathcal{Y}$  exhibits equivariance if it satisfies  $\rho_{\mathcal{Y}}(\mathbf{g}) \cdot f(x) = f(\rho_{\mathcal{X}}(\mathbf{g}) \cdot x), \forall \mathbf{g} \in \mathfrak{G}$ , where  $\rho_{\mathcal{X}}(\mathbf{g})$  and  $\rho_{\mathcal{Y}}(\mathbf{g})$  denote group representations of group element  $\mathbf{g}$  in input and output spaces, respectively. When  $\rho_{\mathcal{Y}}(\mathbf{g})$  is a trivial representation (*i.e.*, always identity transformation), the function  $f$  is invariant to the transformation; otherwise, it is termed equivariant. Hence, invariance can be considered a special case of equivariance. Among those applications in biochemistry, it is a common practice to consider Euclidean transformation (*i.e.*, E(3) Group), including rotation, translation and reflection. Specially owing to the periodic nature of crystalline structures, it is necessary to take periodical translation invariance into account additionally. A thorough discussion of the symmetry considerations is provided as follows:

**O(3)-invariance.** For any rotation/reflection matrix  $\mathbf{O} \in \text{O}(3)$  imposed on the lattice matrix  $\vec{\mathbf{L}}$ , there is  $p(\mathbf{O}\vec{\mathbf{L}}, \mathbf{F}|\mathbf{A}) = p(\vec{\mathbf{L}}, \mathbf{F}|\mathbf{A})$ . The distribution maintains unchanged no matter how the lattice is transformed under O(3) group.

**Periodical translation invariance.** Upon translating all atoms by  $\mathbf{t} \in \mathbb{R}^{3 \times 1}$ , the resulting fractional coordinates are expressed as  $\{\mathbf{F} + \mathbf{t}\mathbf{1}^\top\}$ , with  $\{\cdot\}$  representing the fractional part extraction. Then the equation  $p(\vec{\mathbf{L}}, \{\mathbf{F} + \mathbf{t}\mathbf{1}^\top\}|\mathbf{A}) = p(\vec{\mathbf{L}}, \mathbf{F}|\mathbf{A})$  follows, illustrating the fact that translating the atom coordinates does not affect the distribution.

# 2 Experimental Details

## 2.1 Raw Results of Structure Generation

The finetuning results for various DAO-G configurations on the MP-20 and MPTS-52 datasets are presented in Table 2. Moreover, we pretrain DiffCSP using our CrysDB and present the finetuning results on MP-20 and MPTS-52 in Table 3. We find that pretraining can further improve the performance of DiffCSP, but it is relatively limited compared with our Crysformer-based DAO-G.

**Table 2.** Experimental results (averaged on three runs) for structure generation tasks across different DAO-G configurations. Here, “Stage I” denotes first-stage-only pretraining, “stable” represents pretraining using the 306,830 stable crystals, and “w/ guidance” indicates energy-guided sampling.

	# of samples	MP-20		MPTS-52	
		Match Rate (%) $\uparrow$	RMSE $\downarrow$	Match Rate (%) $\uparrow$	RMSE $\downarrow$
DAO-G (Stage I, Stable)	1	65.63 $\pm$ 0.07	0.0434 $\pm$ 0.0003	31.17 $\pm$ 0.11	0.0790 $\pm$ 0.0015
DAO-G (Stage I)	1	65.60 $\pm$ 0.22	0.0411 $\pm$ 0.0005	32.52 $\pm$ 0.18	0.0731 $\pm$ 0.0008
DAO-G (Stages I+II)	1	<b>65.98 <math>\pm</math> 0.22</b>	<b>0.0402 <math>\pm</math> 0.0013</b>	32.60 $\pm$ 0.10	0.0695 $\pm$ 0.0013
DAO-G (Stages I+II, w/ guidance)	1	<u>65.65 <math>\pm</math> 0.18</u>	<u>0.0406 <math>\pm</math> 0.0014</u>	<b>32.78 <math>\pm</math> 0.06</b>	<b>0.0688 <math>\pm</math> 0.0023</b>

**Table 3.** The mean and standard deviation values of DiffCSP and its pretrained counterpart are reported for the MP-20 and MPTS-52 datasets.

	# of samples	MP-20		MPTS-52	
		Match Rate (%) $\uparrow$	RMSE $\downarrow$	Match Rate (%) $\uparrow$	RMSE $\downarrow$
DiffCSP (w/o pretrain)	1	<b>51.89 <math>\pm</math> 0.30</b>	0.0611 $\pm$ 0.0015	12.15 $\pm$ 0.08	0.1767 $\pm$ 0.0025
DiffCSP (w/ pretrain)	1	50.39 $\pm$ 0.08	<b>0.0563 <math>\pm</math> 0.0011</b>	<b>18.27 <math>\pm</math> 0.20</b>	<b>0.0810 <math>\pm</math> 0.0006</b>

**Table 4.** Experimental results (MAE  $\downarrow$ ) of crystal property prediction on eight datasets.

	MatBench			JARVIS-3D		MP		
	JDFT2D	DIELECTRIC	KVRH	Jarvis_gap	Jarvis_Ehull	Mp_Shear	Mp_Bulk	MP_gap
SchNet	42.663	0.327	<u>0.059</u>	0.430	0.140	0.099	0.066	0.345
CGCNN	49.244	0.598	0.071	0.410	0.170	0.077	0.047	0.292
MEGNet	54.171	0.339	0.066	0.340	0.084	0.099	0.060	0.307
ALIGNN	43.424	0.344	<b>0.056</b>	0.310	0.076	0.078	0.051	0.218
Matformer	47.696	0.681	0.062	0.300	0.064	0.073	0.043	<u>0.211</u>
PotNet	-	-	-	<u>0.270</u>	<u>0.055</u>	<u>0.065</u>	0.040	<b>0.204</b>
Crystal Twins	44.353	0.427	0.066	0.390	0.140	0.082	0.050	0.291
MMPT	<u>38.213</u>	<u>0.324</u>	<b>0.056</b>	<b>0.260</b>	0.061	0.072	<b>0.038</b>	<b>0.204</b>
CrysGNN	-	-	-	0.325	0.083	-	-	0.253
DAO-P	<b>34.280</b>	<b>0.283</b>	0.061	0.273	<b>0.046</b>	<b>0.064</b>	<u>0.040</u>	0.275

## 2.2 Raw Results of Property Prediction

For the property prediction downstream tasks, we compare DAO-P with other predictive models. The raw results are shown in Table 4.

## 2.3 More Results of Superconductor Validation

### 2.3.1 Implementation Details

We begin with a brief overview of the SuperCon dataset [1]. This dataset contains approximately 33,000 superconductors, providing only their chemical formulas and corresponding critical temperatures  $T_c$ . A recent curation effort [11] identified structures for some of these superconductors within the ICSD database [7], creating a structural subset called SuperCon3D. Our focus on ordered superconductors yields a dataset of 1017 structural entries (SC-s) and 748 entries without associated structures (SC-ns).



**Table 5.** The best configuration of each model and the corresponding MAE (logK).

Model	LR	Decay	Fold 1	Fold 2	Fold 3	Fold 4	Fold 5	Average
DAO-P (w/o aug.)	2e-4	5e-5	0.832	0.725	0.691	0.748	0.741	0.747
DAO-P (aug.)	4e-4	5e-5	<b>0.827</b>	<b>0.694</b>	<b>0.640</b>	<b>0.691</b>	<b>0.694</b>	<b>0.709</b>

**Table 6.**  $T_c$  prediction results on three real-world superconductors.

Formula	Experimental $T_c$ (K)	Predicted $T_c$ (K)	Absolute Error (K)
CsV <sub>3</sub> Sb <sub>5</sub> [23]	2.30	2.26	0.04
Zr <sub>16</sub> Pd <sub>8</sub> O <sub>4</sub> [73]	2.73	2.99	0.26
Zr <sub>16</sub> Rh <sub>8</sub> O <sub>4</sub> [73]	3.73	3.77	0.04

To evaluate the ability of DAO-P to predict superconductors  $T_c$ , we perform 5-fold cross-validation on SC-s and the model is referred to as DAO-P (w/o aug.). It is worthwhile to investigate whether SC-n<sub>s</sub> can contribute to enhanced performance. We explore this possibility by employing a cooperative approach between DAO-G and DAO-P. Specifically, we finetune the pretrained DAO-G on the full SC-s, adapting its generative capabilities to superconductor domain. This allowed us to generate structures for the SC-n<sub>s</sub> entries, enriching the training data for each fold. The model finetuned on the augmented dataset is denoted as DAO-P (aug.). The whole process is depicted in Fig. 5(a). For each of the two configurations, we conduct a grid search over learning rates (2e-4, 3e-4, and 4e-4) and weight decay values (1e-5, 2e-5, 3e-5, and 5e-5), and then select the respective best model for comparison in Table 5. As expected, the augmentation with generated structures significantly improves the performance of DAO-P, resulting in the best performance on all five folds.

Additionally, we extend our experiments to three recently discovered superconductors (Fig. 5(d)), utilizing the previously finetuned DAO-G and DAO-P (aug.) models. We first employ the ensembled DAO-P to predict  $T_c$  for them and the results on Table 6 indicates the predicted  $T_c$  are consistent with the experimentally determined values. Then DAO-G is used to generate structures for the three superconductors, given only their formulas, with sample sizes ranging from 1 to 20 in increments of 5. Fig. 5(d, third row) shows the RMSEs for each sample size, demonstrating a clear downward trend with increasing sample size. Notably, we achieve a 2/3 hit rate with just one sample. Further, we select the sample with the lowest RMSE from the generated 20 samples for each superconductor, and visualize them in the second row of Fig. 5(d). Impressively, all three generated structures show excellent agreement with the ground truth structures. These findings suggest that models finetuned on SuperCon exhibits strong generalization to newly discovered superconductors.

### 2.3.2 DFT Results for Three Real-World Superconductors

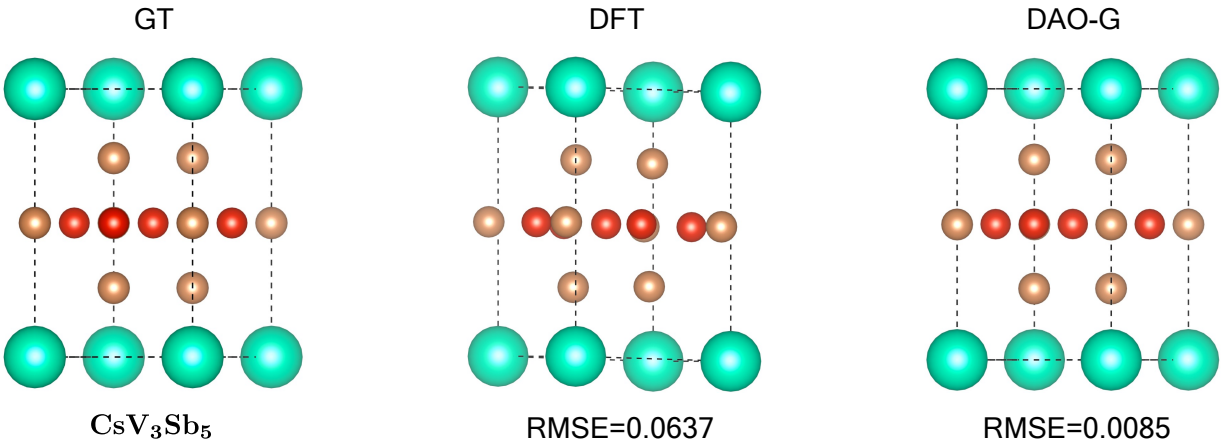
We additionally employ the Quantum-Espresso software (QE [26]), a prevailing DFT tool, to calculate the relaxed structures for the three real-world superconductors. The configurations of QE calculation are presented in Table 7. To ensure a fair comparison, the input structures are randomly initialized, consistent with our diffusion-based generation process. However, all three generation attempts are unsuccessful. We hypothesize that this failure stems from the structural complexity of these superconductors. Therefore, to reduce the computational burden, we perturb the ground truth structures slightly before employing them as starting points for QE calculations. Specifically, we apply 10% lattice lengths perturbation, 10-degree angles perturbation, and 0.1

**Table 7.** The configurations of DFT calculation.

system				electrons		cell		ions
ecutwfc	occupations	smearing	degauss	conv_thr	press_conv_thr	cell_dynamics	ion_maxstep	
40.0	smearing	gaussian	0.01d0	1.0d-6	0.5	bfgs	50 (default)	

**Table 8.** A comparison between DFT tools and our DAO-G on the generation of the superconductor  $\text{CsV}_3\text{Sb}_5$  [23].

Method	Initialized Structure	RMSE	Iterations	Running Time
Quantum-Espresso [26]	slight perturbation on the experiment structure (10% noise for $abc$ , $10^\circ$ noise for $\alpha\beta\gamma$ , 0.1 noise for $\mathbf{F}$ )	0.0637	49 scf-steps + 48 bfgs-steps	4h13m
DAO-G	absolute noises sampled from $\mathcal{U}(0, 1)$ and $\mathcal{N}(\mathbf{0}, \mathbf{I})$	0.0085	1000	5m

**Figure 6.** An illustration of the structure relaxed by DFT and the structure generated by DAO-G, for the superconductor  $\text{CsV}_3\text{Sb}_5$  [23].

fractional coordinates deviation. Only four out of ten runs of  $\text{CsV}_3\text{Sb}_5$  [23] succeeds, with the best achieving an RMSE of 0.0637 compared to DAO-G’s 0.0085. The visualization results are depicted in Fig. 6. Clear discrepancies exist between the relaxed structure and the ground truth, while the structure generated by DAO-G shows well alignment. Regarding efficiency, DAO-G is approximately 50 times faster than DFT calculations. DAO-G generates a structure in 5 minutes, while QE requires approximately 4 hours and 13 minutes. The comparison is presented in Table 8. For the two more complex superconductors ( $\text{Zr}_{16}\text{Pd}_8\text{O}_4$  [73] and  $\text{Zr}_{16}\text{Rh}_8\text{O}_4$  [73]), even slight perturbations similar to those applied to  $\text{CsV}_3\text{Sb}_5$  results in computational exceptions. Subsequently, we further decreased the perturbations to 5% for lattice parameters, 3 degrees for angles, and a standard deviation of 0.05 for fractional coordinates. However, this still leads to prohibitively long computation times (approximately 8 hours per iteration) and prevents convergence within an acceptable time limit.

## 2.4 Implementation of Energy-Guided Sampling

For implementation, we adapt the energy guidance strength using the property optimization method from DiffCSP [35]. Two distributions are shown in Fig. 7: the data distribution (left) and the Boltzmann-augmented distribution (right). Standard sampling techniques, which prioritize high-probability regions within the data distribution, may not be suitable for capturing the Boltzmann

distribution. By incorporating energy guidance, we can effectively sample from a distribution that respects both. Algorithm 1 could provide better understanding.

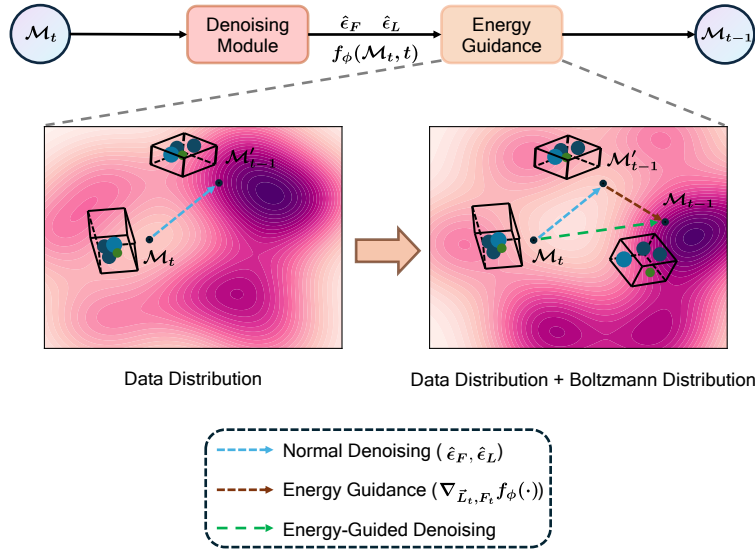


**Figure 7.** The illustration of energy guidance process. The blue arrow represents standard denoising based on the data distribution, which, however, not lies within stable regions. The brown arrow indicates the influence of energy guidance, steering the generation towards the equilibrium distribution. The resulting energy-guided denoising is depicted by the green arrow.

## 2.5 Pretraining Dataset Deduplication

When pretraining DAO-G, we curated the pretraining dataset by removing any samples included in MP-20 and MPTS-52 test sets, thus mitigating the risk of data leakage and ensuring a robust evaluation. The procedure is introduced in Algorithm 2. More stringent thresholds of structure matcher are employed here than in the generation performance evaluation.

## 2.6 Downstream Datasets Introduction

**Matbench [22].** Matbench is a prevailing materials benchmark, tailored for property prediction. It is often used to evaluate various machine learning algorithms. We select JDFT2D [13] to predict Exfoliation Energy, Dielectric [63] to predict Refractive Index and KVRH [20] to predict the average Bulk Moduli. The experimental results are averaged by five folds, which are split by the benchmark in advance.

**Materials Project [33].** The Materials Project is a platform that offers access to computed materials data and advanced analysis tools. We follow the datasets used in MEGNet [10], to predict three properties: Shear Modulus, Bulk Modulus and Bandgap. For generation task, MP-20 and MPTS-52 are both sourced from MP. They are curated to contain stable materials and the atom numbers are less than 20 and 52, respectively.

**JARVIS-3D [14].** We use Jarvis-Tools [15] to download the dft3d dataset. The version is aligned with Matformer [78]. We choose properties of Ehull and Bandgap (MBJ), which are two challenging tasks.

Dataset size and the corresponding hyper-parameters for each one are introduced in Appendix 2.7.

---

**Algorithm 1** Energy-Guided Sampling of DAO-G

---

- 1: **Input:** Pretrained model DAO-P  $f_\phi$  for intermediate energy prediction, denoising model DAO-G  $f_\theta$  for noise prediction, input composition  $\mathbf{A}$ , denoising steps  $T$ , Langevin step size  $\gamma$ , guidance strength  $s$ , coefficient scheduler  $\psi_L$  for lattice and  $\psi_F$  for fractional coordinates.
  - 2: **Output:** Generated Structure  $\mathcal{M} = (\mathbf{A}, \vec{\mathbf{L}}, \mathbf{F})$ .
  - 3: Sample  $\mathbf{F}_T \sim \mathcal{U}(0, 1)$ ,  $\vec{\mathbf{L}}_T \sim \mathcal{N}(\mathbf{0}, \mathbf{I})$ .  $\triangleright$  Initialize  $\mathbf{F}$  and  $\vec{\mathbf{L}}$  from the predefined distributions.
  - 4: **for** step  $t$  in  $T, T-1, \dots, 1$  **do**
  - 5:   Let  $\mathcal{M}_t = (\mathbf{A}, \vec{\mathbf{L}}_t, \mathbf{F}_t)$ .
  - 6:   Sample  $\epsilon_L, \epsilon_F, \epsilon'_F \sim \mathcal{N}(\mathbf{0}, \mathbf{I})$ .
  - 7:    $\hat{\epsilon}_L, \hat{\epsilon}_F \leftarrow f_\theta(\mathcal{M}_t, t)$ .  $\triangleright$  Predict the noises of lattice and coordinates.
  - 8:   Calculate  $\nabla_{\vec{\mathbf{L}}} E, \nabla_{\mathbf{F}} E$  for  $E = f_\phi(\mathcal{M}_t, t)$ .  $\triangleright$  The intermediate energy and gradients.
  - 9:   Acquire  $[\alpha_t, \alpha_{t-1}] = \psi_L([t, t-1])$ ,  $[\sigma_t, \sigma_{t-1}] = \psi_F([t, t-1])$ ,  $\beta_t = 1 - \alpha_t$ ,  $\bar{\alpha}_t = \prod_{\tau=1}^t \alpha_\tau$ .
  - 10:    $\vec{\mathbf{L}}_{t-1} \leftarrow \frac{1}{\sqrt{\alpha_t}}(\vec{\mathbf{L}}_t - \frac{\beta_t}{\sqrt{1-\bar{\alpha}_t}}\hat{\epsilon}_L) - s\beta_t \cdot \frac{1-\bar{\alpha}_{t-1}}{1-\bar{\alpha}_t}\nabla_{\vec{\mathbf{L}}} E + \sqrt{\beta_t \cdot \frac{1-\bar{\alpha}_{t-1}}{1-\bar{\alpha}_t}}\epsilon_L$ .  $\triangleright$  Adding guidance.
  - 11:    $\mathbf{F}_{t-\frac{1}{2}} \leftarrow w(\mathbf{F}_t + (\sigma_t^2 - \sigma_{t-1}^2)\hat{\epsilon}_F - s\frac{\sigma_{t-1}^2(\sigma_t^2 - \sigma_{t-1}^2)}{\sigma_t^2}\nabla_{\mathbf{F}} E + \frac{\sigma_{t-1}\sqrt{\sigma_t^2 - \sigma_{t-1}^2}}{\sigma_t}\epsilon_F)$ .
  - 12:   Let  $\mathcal{M}_{t-\frac{1}{2}} = (\mathbf{A}, \vec{\mathbf{L}}_{t-1}, \mathbf{F}_{t-\frac{1}{2}})$ .  $\triangleright$  Predictor-Corrector for coordinates.
  - 13:    $\_, \hat{\epsilon}_F \leftarrow f_\theta(\mathcal{M}_{t-\frac{1}{2}}, t-1)$ .
  - 14:    $d_t \leftarrow \gamma\sigma_{t-1}/\sigma_1$ .
  - 15:    $\mathbf{F}_{t-1} \leftarrow w(\mathbf{F}_{t-\frac{1}{2}} + d_t\hat{\epsilon}_F + \sqrt{2d_t}\epsilon'_F)$ .
  - 16: **end for**
  - 17: **Return**  $\mathcal{M} = (\mathbf{A}, \vec{\mathbf{L}}_0, \mathbf{F}_0)$ .  $\triangleright$  Return the generated crystal.
- 

---

**Algorithm 2** Deduplication Process for Pretraining Dataset

---

- 1: **Input:** Pretraining Dataset  $\mathbb{D}$ , Test Set  $\mathbb{T}$
  - 2: **Output:** Deduplicated Pretraining Dataset  $\mathbb{D}_{\text{dedup}}$
  - 3: **Define:** SM = Structure-Matcher(stol=0.1, angle\_tol=10, ltol=0.3)  $\triangleright$  Smaller stol
  - 4:  $\mathbb{D}_{\text{dedup}} \leftarrow \emptyset$
  - 5: **for** each sample  $\mathcal{M}_d$  in  $\mathbb{D}$  **do**
  - 6:   **if**  $\mathcal{M}_d.\text{id} \in \mathbb{T}.\text{ids}$  **then**
  - 7:     **continue**  $\triangleright$  Skip samples in the test set
  - 8:   **end if**
  - 9:    $\mathbb{S} \leftarrow \{\mathcal{M} \in \mathbb{T} \mid \mathcal{M}.\text{formula} = \mathcal{M}_d.\text{formula}\}$   $\triangleright$  Find samples with the same formula
  - 10:   overlap-flag  $\leftarrow$  False
  - 11:   **for** each sample  $\mathcal{M}$  in  $\mathbb{S}$  **do**
  - 12:     **if** SM( $\mathcal{M}_d.\text{structure}, \mathcal{M}.\text{structure}$ ) **then**  $\triangleright$  Same formula and similar structures
  - 13:       overlap-flag  $\leftarrow$  True  $\triangleright$  Mark as overlap
  - 14:       **break**  $\triangleright$  No need to check further
  - 15:     **end if**
  - 16:   **end for**
  - 17:   **if not** overlap-flag **then**
  - 18:      $\mathbb{D}_{\text{dedup}} = \mathbb{D}_{\text{dedup}} \cup \{\mathcal{M}_d\}$   $\triangleright$  Add it into the output
  - 19:   **end if**
  - 20: **end for**
  - 21: **Return**  $\mathbb{D}_{\text{dedup}}$   $\triangleright$  Return the deduplicated dataset
-

**Table 9.** Hyper-parameters at pretraing and fine-tuning stages. CrysDB denotes our Pretraining Dataset.

Tasks	Datasets	#Samples	Learning Rate	Weight Decay	Batch Size $\times$ GPUs	Epochs
Pretraining of DAO-P	CrysDB	942,884	2e-4	0	1024 $\times$ 2	800
Pretraining of DAO-G (stage I)	CrysDB (dedup)	919,258	3e-4	0	1024 $\times$ 3	800
Pretraining of DAO-G (stage II)	CrysDB (dedup, relaxed)	919,258	1e-4	0	1024 $\times$ 3	500
Property Prediction	JDFT2D	636	8e-5	5e-5	128 $\times$ 1	300
	DIELECTRIC	4,764	5e-5	5e-5	24 $\times$ 2	300
	KVRH	10,987	8e-5	1e-5	128 $\times$ 1	200
	Jarvis_gap	18,171	1e-4	2e-4	256 $\times$ 2	300
	Jarvis_Ehull	55,370	7e-4	1e-4	256 $\times$ 3	500
	Mp_Shear	5,449	1e-4	2e-5	256 $\times$ 2	500
	Mp_Bulk	5,450	3e-4	0	256 $\times$ 2	500
Structure Generation	MP_gap	69,239	2e-5	0	64 $\times$ 3	300
	MP-20	45,231	2e-5	1e-5	400 $\times$ 8	1000
	MPTS-52	40,476	2e-5	1e-5	80 $\times$ 8	1000

## 2.7 Hyperparameters

The pretrained model comprises 12 layers of our designed Transformer architecture, with a hidden dimension of 384. We configure the model with 8 attention heads and utilize the SiLU activation function. We adopt the Adam optimizer for training the network and utilize a cosine learning rate scheduler with linear warmup for learning rate adjustment, consistent with current trends in large language models (LLMs) training. All experiments are performed on NVIDIA-A100-80G and NVIDIA-4090-24G GPUs. Table 9 outlines specific hyper-parameter configurations during pretraining and finetuning stages.

## 2.8 Configurations of Finetuning

For crystal property prediction downstream tasks, a two-layer MLP (i.e., prediction head) is integrated with the pretrained model, allowing for simultaneous fine-tuning of the entire model. Separate prediction heads are used for each dataset and when training we normalize the property labels to follow a standard normal distribution for better numerical stability. Notably, models for MP\_gap and DIELECTRIC are finetuned on NVIDIA-A100 GPUs due to the memory limitations, and the remaining models are finetuned on NVIDIA-4090 GPUs.

While for structure generation tasks, we finetune the model using the same loss functions as the pretraining. After finetuning, we generate structures with the test set and evaluate them against the ground truth by calculating the match rate and RMSE using the pymatgen library [60], with thresholds stol=0.5, angle\_tol=10, ltol=0.3.

## 2.9 Visualization of the Diffusion Process

To better understand how the structures evolve during the generation process, we select several examples from MP-20 dataset and visualize the perturbed structures at different timesteps in Fig. 8.

## 3 Theoretical Analysis

In this section, we provide rigorous mathematical proofs and detailed derivations for the key theoretical results presented in the main text.



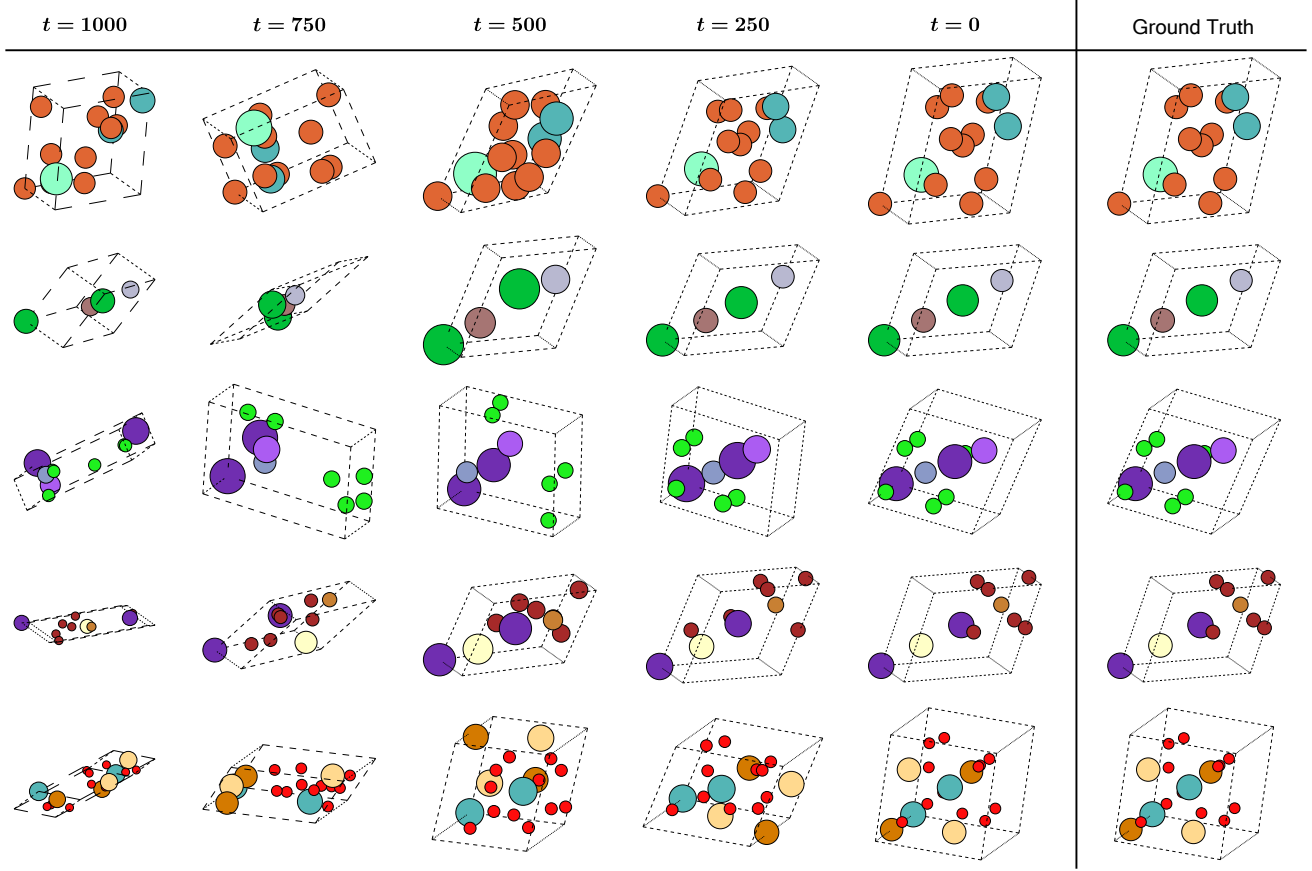


**Figure 8.** Visualization of the generated structures by DAO-G throughout the diffusion process. We show representative structures at timesteps 1000, 750, 500, 250, and 0. The structures at timestep 0 represent the final generated samples, which are well-aligned with the corresponding ground truth structures. To enhance visual clarity and facilitate comparison, a common atom within each group (represented by a row) has been translated to the origin.

### 3.1 Derivation of the Intermediate Energy Prediction Loss

From CEP [50], we know that the intermediate energy  $\mathcal{E}_t(\mathcal{M}_t) = -\log \mathbb{E}_{q_{0t}(\mathcal{M}_0|\mathcal{M}_t)}[e^{-\beta\mathcal{E}_0(\mathcal{M}_0)}]$ , that is  $e^{-\mathcal{E}_t(\mathcal{M}_t)} = \mathbb{E}_{q_{0t}(\mathcal{M}_0|\mathcal{M}_t)}[e^{-\beta\mathcal{E}_0(\mathcal{M}_0)}]$ . To model  $\mathcal{E}_t(\mathcal{M}_t, t)$  for any  $t > 0$ , we design a network  $f_\phi(\mathcal{M}_t, t)$  to approximate it by the loss function showed in Eq. (10). Here we prove this loss function can lead to the objective.

$$\begin{aligned}
\mathcal{L}_{\text{IEP}}(\phi) &= \mathbb{E}_{q_{0t}(\mathcal{M}_0, \mathcal{M}_t)} \left[ \|e^{-f_\phi(\mathcal{M}_t, t)} - e^{-\beta\mathcal{E}_0(\mathcal{M}_0)}\|_2^2 \right] \\
&= \mathbb{E}_{q_{0t}(\mathcal{M}_0, \mathcal{M}_t)} \left[ e^{-2f_\phi(\mathcal{M}_t, t)} - 2e^{-f_\phi(\mathcal{M}_t, t) - \beta\mathcal{E}_0(\mathcal{M}_0)} + e^{-2\beta\mathcal{E}_0(\mathcal{M}_0)} \right] \\
&= \mathbb{E}_{q_{0t}(\mathcal{M}_0, \mathcal{M}_t)} \left[ e^{-2f_\phi(\mathcal{M}_t, t)} \right] - 2\mathbb{E}_{q_{0t}(\mathcal{M}_0, \mathcal{M}_t)} \left[ e^{-f_\phi(\mathcal{M}_t, t) - \beta\mathcal{E}_0(\mathcal{M}_0)} \right] + C_1 \\
&= \mathbb{E}_{q_t(\mathcal{M}_t)} \left[ e^{-2f_\phi(\mathcal{M}_t, t)} \right] - 2\mathbb{E}_{q_t(\mathcal{M}_t)} \mathbb{E}_{q_{0t}(\mathcal{M}_0|\mathcal{M}_t)} \left[ e^{-f_\phi(\mathcal{M}_t, t) - \beta\mathcal{E}_0(\mathcal{M}_0)} \right] + C_1 \\
&= \mathbb{E}_{q_t(\mathcal{M}_t)} \left[ e^{-2f_\phi(\mathcal{M}_t, t)} - 2\mathbb{E}_{q_{0t}(\mathcal{M}_0|\mathcal{M}_t)} \left[ e^{-f_\phi(\mathcal{M}_t, t) - \beta\mathcal{E}_0(\mathcal{M}_0)} \right] \right] + C_1 \\
&= \mathbb{E}_{q_t(\mathcal{M}_t)} \left[ e^{-2f_\phi(\mathcal{M}_t, t)} - 2e^{-f_\phi(\mathcal{M}_t, t)} \mathbb{E}_{q_{0t}(\mathcal{M}_0|\mathcal{M}_t)} \left[ e^{-\beta\mathcal{E}_0(\mathcal{M}_0)} \right] \right] + C_1,
\end{aligned} \tag{12}$$

where  $C_1 = \mathbb{E}_{q_{0t}(\mathcal{M}_0, \mathcal{M}_t)} \left[ e^{-2\beta\mathcal{E}_0(\mathcal{M}_0)} \right]$  is a constant independent of the parameter  $\theta$ , and  $\beta$  is the temperature. The optimal minimum of the loss function  $\mathcal{L}_{\text{IEP}}$  is attained if and only if the

condition  $e^{-f_\phi(\mathcal{M}_t, t)} = \mathbb{E}_{q_{0t}(\mathcal{M}_0|\mathcal{M}_t)}[e^{-\beta\mathcal{E}_0(\mathcal{M}_0)}]$  is satisfied, which indicates that  $f_\phi(\mathcal{M}_t, t)$  serves as an approximation of  $\mathcal{E}_t(\mathcal{M}_t)$ . In the pretraining experiments, we set  $\beta = 1$ .

### 3.2 Invariance of the learned Node Features

In this part, we provide the details why  $\mathbf{H}^{(S)}$  is OP invariant. We use the notation  $\{\cdot\}$  to represent the fractional part extraction. From Appendix A of DiffCSP [35], we can learn that

$$\varphi_{\text{FT}}(\{\mathbf{f}_i + \mathbf{t}\} - \{\mathbf{f}_j + \mathbf{t}\}) = \varphi_{\text{FT}}(\mathbf{f}_i - \mathbf{f}_j). \quad (13)$$

where,  $\mathbf{t}$  is the translation. Then, we prove that the pre-calculated edge feature  $\mathbf{e}_{ij}$  exhibits OP-invariance. Given any rotation/reflection matrix  $\mathbf{O} \in \text{O}(3)$  imposed on the lattice matrix  $\vec{\mathbf{L}}$ , we have:

$$\begin{aligned} \mathbf{e}_{ij}^{\text{transformed}} &= \text{Normalization} \left( (\mathbf{O}\vec{\mathbf{L}})^\top (\mathbf{O}\vec{\mathbf{L}}) \parallel \varphi_{\text{FT}}(\{\mathbf{f}_i + \mathbf{t}\} - \{\mathbf{f}_j + \mathbf{t}\}) \right), \\ &= \text{Normalization} \left( \vec{\mathbf{L}}^\top (\mathbf{O}^\top \mathbf{O}) \vec{\mathbf{L}} \parallel \varphi_{\text{FT}}(\mathbf{f}_i - \mathbf{f}_j) \right) \\ &= \text{Normalization} \left( \vec{\mathbf{L}}^\top \vec{\mathbf{L}} \parallel \varphi_{\text{FT}}(\mathbf{f}_i - \mathbf{f}_j) \right) \\ &= \mathbf{e}_{ij}. \end{aligned} \quad (14)$$

Moreover, the node feature  $\mathbf{h}_i^{(0)}$  is OP-invariant, because it is initialized by CGCNN embedding, depending solely on the atom type  $\mathbf{a}_i$ . Therefore, the inputs (i.e.  $\mathbf{E}, \mathbf{H}^{(0)}$ ) to our noise prediction model are all OP-invariant. Since the components of our Transformer block, including multi-head attention and feedforward layers, operate exclusively on OP-invariant features, the final output  $\mathbf{h}_i^{(S)}$  is also OP-invariant.

### 3.3 Equivariance of the Noise Output

For fractional coordinates, we compute the noise by  $\hat{\epsilon}_F(\mathcal{M}_t, t) = \varphi_F(\mathbf{H}_t^{(S)})$ . As we have proved that  $\mathbf{H}_t^{(S)}$  is OP-invariant in Appendix 3.2, it is obvious that the predicted  $\hat{\epsilon}_F(\mathcal{M}_t, t)$  also meets OP-invariance. In terms of the lattice noise, we just need to consider O(3) transformation. For  $\hat{\epsilon}_L(\mathcal{M}_t, t) = \vec{\mathbf{L}}\varphi_L(\bar{\mathbf{h}}_t)$ , if we impose an O(3) transformation  $\mathbf{O}$  on the crystal,  $\bar{\mathbf{h}}_t$  remains unchanged and the lattice representation becomes  $\mathbf{O}\vec{\mathbf{L}}$ . We derive the transformed score:

$$\begin{aligned} \hat{\epsilon}_L^{\text{transformed}}(\mathcal{M}_t, t) &= (\mathbf{O}\vec{\mathbf{L}})\varphi_L(\bar{\mathbf{h}}_t) \\ &= \mathbf{O} \left( \vec{\mathbf{L}}\varphi_L(\bar{\mathbf{h}}_t) \right) \\ &= \mathbf{O}\hat{\epsilon}_L(\mathcal{M}_t, t). \end{aligned} \quad (15)$$

It indicates that the noise  $\hat{\epsilon}_L(\mathcal{M}_t, t)$  is also transformed given the transformation on the input crystal. That is, the predicted score for lattice is O(3) equivariant. Since the crystal representation  $\bar{\mathbf{h}}_t$  is OP-invariant, the energy output  $\varphi_E(\bar{\mathbf{h}}_t)$  maintains OP-invariance as well.